Received: 25 January 2022 | Revised: 27 February 2023 | Accepted: 24 April 2023

DOI: 10.33012/navi.603

ORIGINAL ARTICLE

# Closed-Form Study of Undetected Range Errors Induced by Ionospheric Anomalies for GAST-D GBAS

**Wang Li**[1] | **Yiping Jiang***[1]

[1] Department of Aeronautical and Aviation Engineering, The Hong Kong Polytechnic University, Hong Kong, SAR, China

**Correspondence**
Yiping Jiang
Department of Aeronautical and Aviation Engineering, The Hong Kong Polytechnic University, Hong Kong, SAR, China.
Email: yiping.jiang@polyu.edu.hk

**Abstract**

In ground-based augmentation system (GBAS) approach service type D (GAST-D), various ionospheric monitors are implemented in both aircraft and ground facilities to detect ionospheric anomalies. Additionally, the largest undetected differential range errors induced by ionospheric anomalies must be examined because these errors are used in geometry screening to identify potentially unsafe satellite geometries. Based on the ionospheric front threat model, a closed-form expression of the largest undetected ionospheric range error has been established for GBAS approach service type C (GAST-C), where only ground ionospheric monitoring is involved. This paper presents a closed-form expression for GAST-D, and both the ionospheric front model and plasma bubble threat model are taken into consideration. Based on exhaustive simulations among all possible ionospheric threat conditions, the expression is determined as a linear function of the relative speed and gradient magnitude of the ionospheric anomaly. Compared with the linear expression of ionospheric errors for GAST-C, the expression for GAST-D demonstrates that the use of additional ionospheric monitors and a smaller time constant for the code-carrier smoothing filter can effectively reduce the largest undetected ionospheric range error.

**Keywords**

GBAS, integrity risk, ionospheric anomaly

## 1 | INTRODUCTION

Located at heights between approximately 50 km and 1000 km, the ionosphere is a shell of dispersive medium that contains electrons and electrically charged atoms (Misra & Enge, 2004). As global positioning system (GPS) signals travel through the ionosphere, they experience a delay, which is proportional to the density of total electron content. A ground-based augmentation system (GBAS) augments existing GPS signals by broadcasting differential corrections and integrity information to enable precision approaches for aircraft (Hoffmann & Walton, 2018). Under nominal conditions, the ionospheric delay is partly eliminated by differential corrections, and residual ionospheric errors caused by spatial decorrelation between the ground and aircraft are bounded by the integrity parameter $\sigma_{vig}$ (Chang et al., 2021). However, in the case of an ionospheric anomaly, the spatial decorrelation might become too large to be bounded. For such cases, ionospheric monitors come into play. Still, undetected errors always exist, which may induce large vertical position errors, thus posing a risk to user safety.

One way to mitigate this threat is by screening out potentially unsafe satellite geometries, known as geometry screening (Pullen et al., 2009). A satellite geometry is unsafe if it has an unacceptably large position error induced by a hypothetical worst-case ionospheric anomaly, even if it has an acceptable vertical protection level (VPL). Unsafe satellite geometries are screened out by inflating $\sigma_{vig}$ to ensure that the VPL exceeds the vertical alert limit and to thus ensure that all unsafe geometries are unusable (Lee et al., 2011). With the geometry screening procedure, the largest ionosphere-induced differential range error (*Er*) must be determined in order to compute the worst-case ionosphere-induced position error. Previously, *Er* has been obtained by exhaustive simulations under specific scenarios and parameter ranges. The results are then used to generate look-up tables for future reference (Lee et al., 2006). This process involves uncertainty and low efficiency, as the exhaustive simulations must be repeated if the scenario or parameter ranges change. Kim et al. (2021) proposed a closed-form expression as a bound for all possible scenarios and parameter ranges, provided in the form of a linear function of the gradient and relative speed of the ionospheric anomaly. The expression established for GBAS approach service type C (GAST-C) is based on the ionospheric front model used to describe mid-latitude ionospheric anomalies. In GAST-C, a code-carrier divergence (CCD) monitor is applied on the ground to detect ionospheric anomalies for category I precision approaches (Simili & Pervan, 2006). The geometry screening method is implemented at the ground station and must screen out all potentially unsafe satellite geometries that users might experience.

GBAS approach service type D (GAST-D), which has stricter performance requirements, was proposed to support more demanding CAT II/III precision approaches. This paper focuses on establishing a linear closed-form expression of the largest undetected ionosphere-induced differential range error for GAST-D. In GAST-D, the responsibility of detecting ionospheric anomalies is shared between the aircraft and ground. A CCD monitor and an ionosphere gradient monitor (IGM) are implemented on the ground, whereas dual-solution pseudorange ionospheric gradient monitoring (DSIGMA) is implemented on the aircraft (RTCA DO-253D, 2017). Moreover, geometry screening is transferred to the aircraft to make use of the known aircraft satellite geometries, which simplifies the screening procedure (Lee et al., 2011; ICAO, 2018). This transfer also improves availability because it avoids the conservatism implied by the ground, aiming to ensure that all possible subset geometries are safe for the aircraft (Marini-Pereira et al., 2021). The satellite geometry screening in GAST-D GBAS is completely different from the ground geometry screening previously described for GAST-C GBAS. The vertical projection factor for satellites is evaluated by comparing $\max(s_{vert_2}) \times E_{IG}$ with $\max(E_v)$, where $s_{vert_2}$ is the sum of the two largest absolute elements of the vertical projection matrix $s_{vert}$ and $E_{IG}$ and $\max(E_v)$ are the maximum value of the ionospheric gradient error and user-specified values for the vertical position error limit, respectively (RTCA DO-253D, 2017). The satellite geometries are screened out when $\max(s_{vert_2}) \times E_{IG}$ is larger than $\max(E_v)$. $E_{IG}$ is calculated on the aircraft by adding $Y_{EIG}$ and the product of $M_{EIG}$ and the distance from the GBAS reference point to the runway threshold. The parameters $Y_{EIG}$ and $M_{EIG}$ in message type 2 are broadcasted by the GBAS ground station. The first parameter, $Y_{EIG}$, is the maximum value of the ionospheric gradient error at the GBAS reference point, and the second parameter, $M_{EIG}$, is the slope of the maximum ionospheric gradient error versus distance (ICAO, 2018). The values of $Y_{EIG}$ and $M_{EIG}$ must be determined to ensure that all predetermined potentially undetected Er values remain below $E_{IG}$.

Using a technique similar to that for GAST-C (Kim et al., 2021), this paper presents a method for generating the largest undetected *Er* for GAST-D in order to help determine $E_{IG}$ for each threshold and to determine $Y_{EIG}$ and $M_{EIG}$. A closed-form expression of the largest *Er* as a linear function of the ionospheric gradient and speed is given in this paper. Different from the expression for GAST-C, the derivation of the closed-form expression for GAST-D GBAS considers both the ionospheric front model and plasma bubble model; moreover, ionospheric monitors are distributed on both the ground and aircraft.

This paper is organized as follows. First, the geometric models of impact scenarios under an ionospheric front and plasma bubble are described. Then, an explicit expression of *Er* induced by an ionospheric anomaly is derived, followed by an analysis of ionospheric monitors to obtain undetected ionosphere-induced errors. Finally, the closed-form expression that bounds the largest undetected *Er* is derived based on exhaustive simulation results.

## 2 | IONOSPHERIC IMPACT SCENARIOS

Researchers have studied the characteristics of ionospheric anomalies in mid-latitude and low-latitude regions, e.g., the continental United States (Lee et al., 2017), Europe (Robert et al., 2018), Brazil (Lee et al., 2015), and the Asia-Pacific region (Saito & Yoshihara, 2017). Two types of simplified threat models, i.e., the wedge model and trapezoid model, have been used to describe the ionospheric front and plasma bubble, respectively (Pullen et al., 2009; Saito et al., 2009; Saito et al., 2017). The wedge model used to describe an ionospheric front contains three parameters: the gradient, i.e., the linear change between the maximum ionospheric delay and nominal ionospheric delay, $g$; the front width, $w$; and the front propagation speed relative to the speed of the ionospheric pierce point of ground ($IPP_{GF}$), $\Delta v_m$. The trapezoid model for a plasma bubble is formed by a pair of wedges, which contains seven parameters: a pair of gradients, $g_1$, $g_2$; the width of each wedge, $w_1$, $w_2$; the width of plasma bubble depletion, $w_b$; and the speed of the plasma bubble relative to the speed of $IPP_{GF}$, $\Delta v_l$. The total differential delay is assumed to be the same on both sides of the plasma bubble ($Depth = g_1 w_1 = g_2 w_2$).

The geometries of the aircraft and ground under the impact of a moving ionospheric front and plasma bubble are shown in Figures 1 and 2. To fully examine the

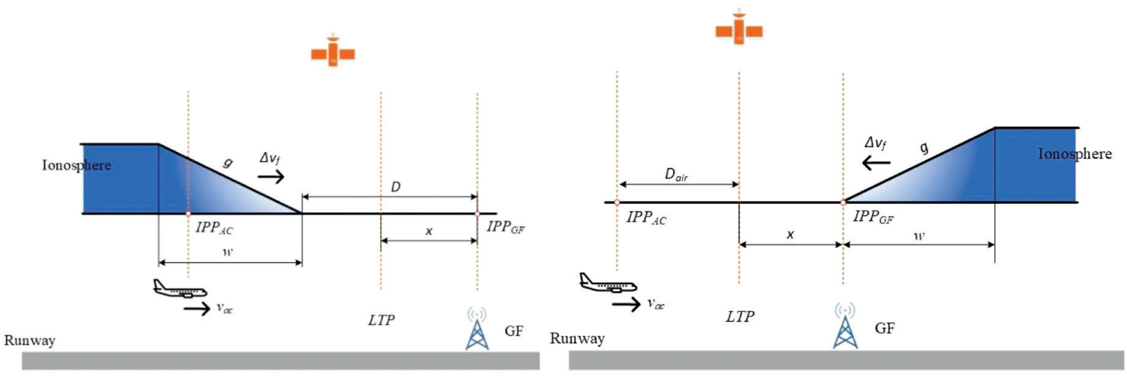


(a) (b)

**FIGURE 1** Geometry model for the aircraft and ground under an ionospheric front (a) Ahead case with the aircraft and front moving in the same direction (b) Behind case with the aircraft and front moving in opposite directions impact of the ionospheric front and plasma bubble, an “ahead case” and a “behind case” are considered in the scenarios. In the ahead case, the aircraft and ionospheric anomaly are assumed to move in the same direction, and the ionospheric anomaly affects the aircraft prior to the ground. In contrast, in the behind case, the ionospheric anomaly and the aircraft are assumed to move in opposite directions, and the ground is affected by the anomaly prior to the aircraft.

During the approach, the aircraft is assumed to move at a constant velocity of $v_{ac}$ (70 m/s) parallel to the runway toward the landing threshold point (LTP), which is assumed to be located at a distance of $x = 5$ km from the centroid of the ground. Because the distances from the aircraft and ground to their corresponding IPPs ($IPP_{AC}$ and $IPP_{GF}$) are much smaller than their distances to satellites, the relative speed between $IPP_{AC}$ and $IPP_{GF}$ is assumed to be equal to $v_{ac}$. $D$ denotes the initial distance between the ionospheric anomaly and the ground in the ahead case. $D_{air}$ denotes the initial distance between the LTP and the aircraft in the behind case. The parameters shown in Figures 1 and 2 are assumed to remain constant during the aircraft approach.

The generation of undetected $Er$ ($Er_{undetected}$) for GAST-D is shown in Figure 3. The ionospheric delays for the aircraft ($I_{AC}$) and ground ($I_{GF}$) pass through carrier smoothing code (CSC) filters, and $Er$ is calculated from the difference between

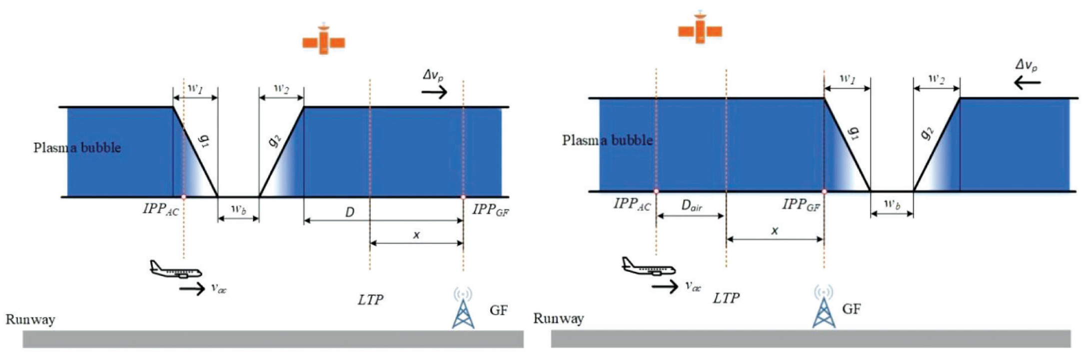


(a) (b)

**FIGURE 2** Geometry model for the aircraft and ground under a plasma bubble (a) Ahead case with the aircraft and bubble moving in the same direction (b) Behind case with the aircraft and bubble moving in opposite directions

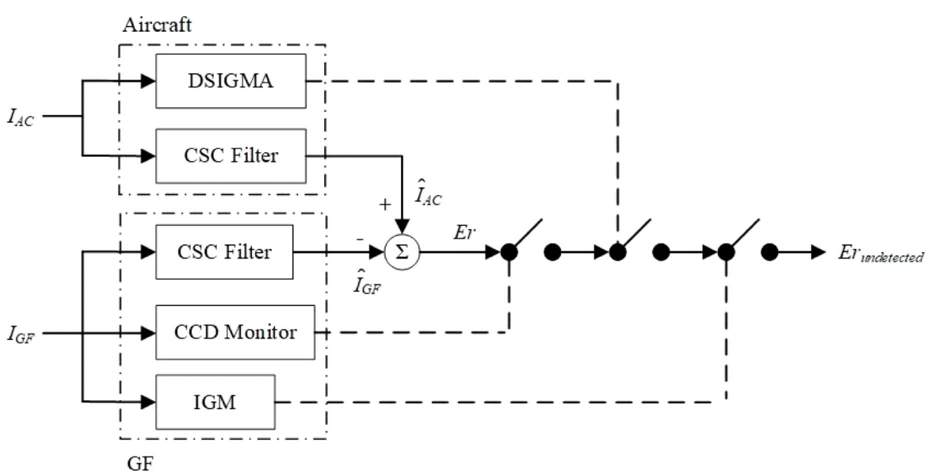


**FIGURE 3** Diagram of $Er_{undetected}$ generation caused by an ionospheric anomaly

two CSC filter outputs ($\hat{I}_{AC}$ and $\hat{I}_{GF}$). When all ionospheric monitors fail to detect the ionospheric anomaly with the required probability, the $Er$ at the LTP is recorded as $Er_{undetected}$.

## 3 | EXPLICIT EXPRESSION OF DIFFERENTIAL RANGE ERRORS

$Er$ is computed by subtracting $\hat{I}_{GF}$ from $\hat{I}_{AC}$:

$$Er = \hat{I}_{AC} - \hat{I}_{GF} \tag{1}$$

$I_{AC}$, $I_{GF}$, and the CSC filter are analyzed first. The relevant variables and their definitions are listed in Table 1.

### 3.1 | Ionospheric Delay

$I_{AC}$ and $I_{GF}$ are determined by the position of $IPP_{AC}$ and $IPP_{GF}$ relative to the ionospheric front or plasma bubble. Because the aircraft and ionospheric anomaly

**TABLE 1**
Nomenclature

| Symbol | Description | Unit |
|---|---|---|
| $t$ | Time | s |
| $g$ | Magnitude of the gradient of the ionospheric front model | mm/km |
| $g_1(g_2)$ | Magnitude of the left (right) gradient of the plasma bubble model | mm/km |
| $w$ | Width of the ionospheric front model | km |
| $w_1(w_2)$ | Width of the left (right) depletion of the plasma bubble model | km |
| $v_{ac}$ | Aircraft speed (70 m/s) | m/s |
| $\Delta v_m$ | Propagation speed of the ionospheric front relative to $IPP_{GF}$ | m/s |
| $\Delta v_l$ | Propagation speed of the plasma bubble relative to $IPP_{GF}$ | m/s |
| $x$ | Distance between the LTP and ground | km |
| $D$ | Initial distance between the ground and ionospheric front or plasma bubble in the ahead case | km |
| $D_{air}$ | Initial distance between the LTP and aircraft in the behind case | km |
| $I$ | Ionospheric delay | m |
| $\hat{I}$ | Ionospheric delay after the CSC filter | m |
| $T$ | Time period to pass the slope of the ionospheric anomaly | s |
| $t_{GF}$ | Time at which the ionospheric anomaly starts to affect the ground | s |
| $t_{AC}$ | Time at which the ionospheric anomaly starts to affect the aircraft | s |
| $t_{LTP}$ | Time period for the aircraft to arrive at the LTP | s |
| $Out_{dsigma}$ | Output of the DSIGMA monitor | m |
| $Out_{ccd}$ | Output of the CCD monitor | m/s |
| $Out_{igm}$ | Output of the IGM | mm/km |
| $Er$ | Differential range error | m |

Note: For a given symbol, e.g., $I_{l,AC}^{ah,fa}$, the indexes indicate the plasma bubble located in low-latitude regions $l$, for aircraft $AC$, in the ahead case $ah$, under the fast-moving scenario $fa$. If one of the indexes is missing, then the parameter is not related to that index.

move in the same direction in the ahead case, slow-moving and fast-moving scenarios are considered in order to ensure that the aircraft experiences the entire ionospheric delay during the approach. In the slow-moving scenario, the speed of the ionospheric anomaly relative to $IPP_{GF}$ is less than the speed of the aircraft, i.e., $\Delta v_m < v_{ac}$, $\Delta v_l < v_{ac}$, and the $IPP_{AC}$ at the beginning of the approach is assumed to occur at the rear edge of the ionospheric front model or plasma bubble model, as shown in Figure 4(a) and Figure 5(a). In contrast, the $IPP_{AC}$ at the beginning of the approach is assumed to be at the front edge of the ionospheric front model or plasma bubble model under the fast-moving scenario with $\Delta v_m > v_{ac}$, $\Delta v_l > v_{ac}$. The geometric models of fast-moving scenarios are shown in Figure 4(b) and Figure 5(b). In the behind case, $IPP_{GF}$ is assumed to occur at the rear edge of the ionospheric front model or plasma bubble model, as shown in Figure 6 and Figure 7. The explicit expressions of $I_{AC}$ and $I_{GF}$ for the ionospheric front model and plasma bubble model in the ahead and behind cases are derived as follows.

The derivation of $I_{AC}$ and $I_{GF}$ under the ionospheric front model in the ahead case is the same as in GAST-C (Kim et al., 2021). The temporal changes in $I_{AC}$ and $I_{GF}$ are shown in Figure 4. $g_{AC}$ and $g_{GF}$ are the temporal gradients for the aircraft and ground, respectively; $T_{AC}$ and $T_{GF}$ are the time periods for the aircraft IPP and ground IPP to pass through the entire slope of the ionospheric front, respectively; $t_{LTP}$ is the time period for the aircraft to arrive at the LTP; $t_{GF}$ is the time period before the ionospheric front starts to affect the ground. Using the unit step function $u(t)$, $I_{AC}$ for the slow-moving and fast-moving scenarios in the ahead case, $I^{ah,sl}_{m,AC}$ and $I^{ah,fa}_{m,AC}$, can be expressed as follows (Kim et al., 2021):

$$
\begin{aligned}
I^{ah,sl}_{m,AC}(t) &= g^{ah}_{m,AC}\left[T_{m,AC} - \left\{R(t) - R\left(t - T_{m,AC}\right)\right\}\right] \\
I^{ah,fa}_{m,AC}(t) &= g^{ah}_{m,AC}\left\{R(t) - R\left(t - T_{m,AC}\right)\right\}
\end{aligned}
\tag{2}
$$

where $t$ indicates the current time, $R(t) = tu(t)$ is a ramp function, the subscript $m$ indicates the ionospheric front model, the superscripts *sl* and *fa* indicate the slow-moving and fast-moving scenarios, respectively, and the superscript *ah* indicates the ahead case. Moreover, $I_{GF}$ for the slow-moving and fast-moving scenarios, $I^{ah,sl}_{m,GF}$ and $I^{ah,fa}_{m,GF}$, can be expressed as follows:

$$
I^{ah,sl}_{m,GF}(t) = I^{ah,fa}_{m,GF}(t) = g^{ah}_{m,GF}\left\{R\left(t - t_{m,GF}\right) - R\left(t - t_{m,GF} - T_{m,GF}\right)\right\}
\tag{3}
$$

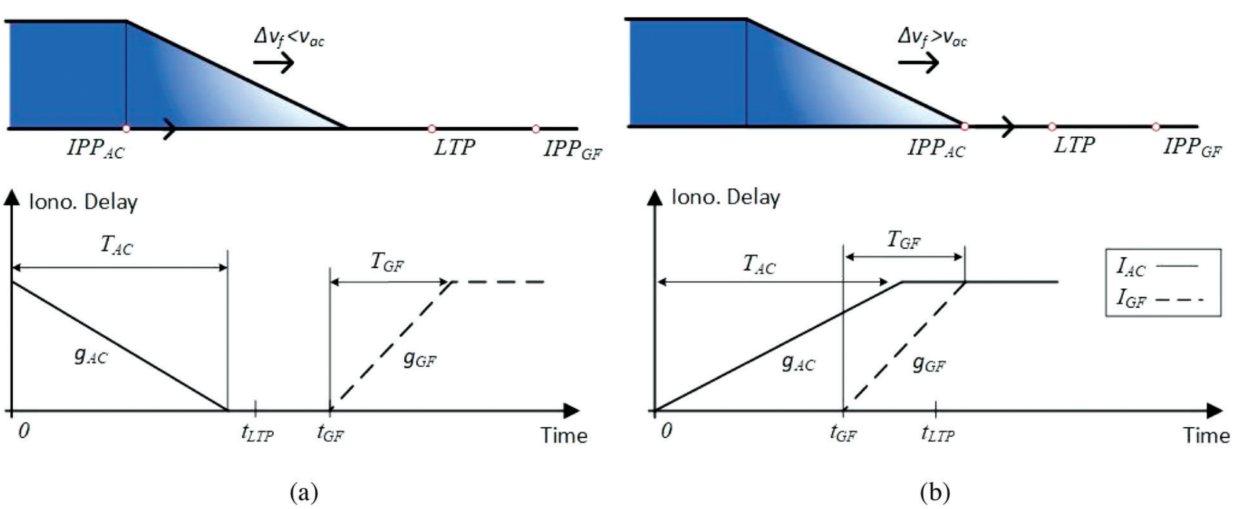


**FIGURE 4** $I_{AC}$ and $I_{GF}$ under an ionospheric front in the ahead case (Kim et al., 2021) (a) slow-moving scenario (b) fast-moving scenario

The relevant parameters are calculated as follows (Kim et al., 2021):

$$t_{m,GF} = \frac{D}{\Delta v_m}, \; T_{m,GF} = \frac{w}{\Delta v_m}, \; T_{m,AC} = \frac{w}{\left|\Delta v_m - v_{m,AC}\right|} \tag{4}$$

$$g^{ah}_{m,AC} = g\left|\Delta v_m - v_{AC}\right|, \; g^{ah}_{m,GF} = g\Delta v_m \tag{5}$$

$$t^{ah,sl}_{m,LTP} = \frac{D+w-x}{v_{AC}}, \; t^{ah,fa}_{m,LTP} = \frac{D-x}{v_{AC}} \tag{6}$$

This paper also considers $I_{AC}$ and $I_{GF}$ under the ionospheric front model in the behind case, as shown in Figure 6. $t_{AC}$ is the time at which the ionospheric front starts to impact the aircraft. For the ionospheric front model in the behind case, $I_{AC}$ and $I_{GF}$ are denoted as $I^{be}_{m,AC}$ and $I^{be}_{m,GF}$, respectively:

$$\begin{aligned} I^{be}_{m,AC}(t) &= g^{be}_{m,AC}\left\{R\left(t-t_{m,AC}\right)-R\left(t-t_{m,AC}-T_{m,AC}\right)\right\} \\ I^{be}_{m,GF}(t) &= g^{be}_{m,GF}\left\{R(t)-R\left(t-T_{m,GF}\right)\right\} \end{aligned} \tag{7}$$

where the superscript *be* indicates the behind case. The related parameters are calculated as follows:

$$g^{be}_{m,AC} = g\left(\Delta v_m + v_{AC}\right), \; g^{be}_{m,GF} = g\Delta v_m \tag{8}$$

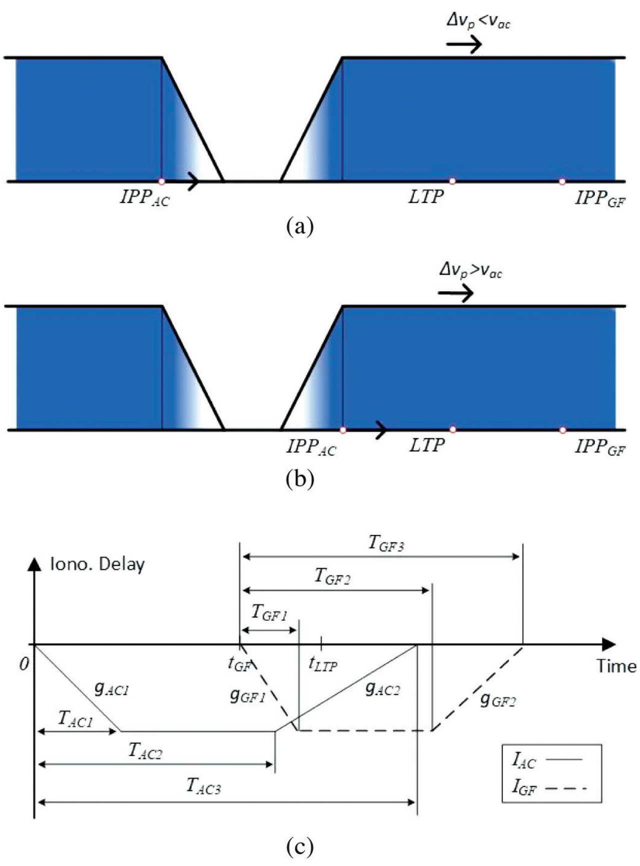


**FIGURE 5** $I_{AC}$ and $I_{GF}$ for the plasma bubble model in the ahead case (a) slow-moving scenario (b) fast-moving scenario (c) ionospheric delay for aircraft and GF

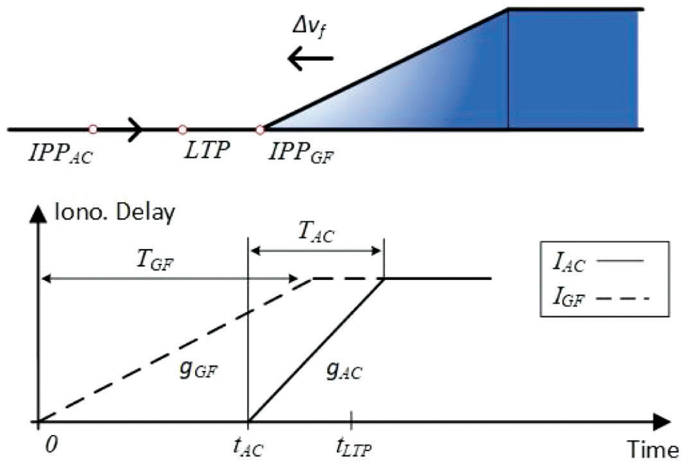


**FIGURE 6** $I_{AC}$ and $I_{GF}$ under an ionospheric front in the behind case

$$t_{m,AC} = \frac{D_{air}}{v_{AC}},\ t_{m,LTP}^{be} = \frac{D_{air} + x}{\Delta v_m + v_{AC}} \tag{9}$$

The threat model of a plasma bubble is also studied in this paper, where the temporal change in $I_{AC}$ and $I_{GF}$ follows the same trend under slow-moving and fast-moving scenarios in the ahead case, as shown in Figure 5. $T_{AC1}$, $T_{AC2}$, and $T_{AC3}$ are the time periods for the aircraft IPP to pass through the nearest slope, depletion, and farthest slope, respectively; $T_{GF1}$, $T_{GF2}$, and $T_{GF3}$ are the time periods for the ground IPP to pass through the nearest slope, depletion, and farthest slope, respectively. $g_{AC1}$ and $g_{AC2}$ are the temporal gradients for the aircraft when its IPP is under the nearest and farthest slopes, respectively. $g_{GF1}$ and $g_{GF2}$ are the temporal gradients for the ground when its IPP is under the nearest and farthest slopes. For the slow-moving and fast-moving scenarios in the plasma bubble model, $I_{AC}$ is denoted as $I_{l,AC}^{ah,sl}$ and $I_{l,AC}^{ah,fa}$, respectively. The expressions are defined with $u(t)$:

$$\begin{aligned} I_{l,AC}^{ah,sl}(t) &= -g_{l,AC1}^{ah,sl}\left\{R(t) - R\left(t - T_{l,AC1}^{ah,sl}\right)\right\} + g_{l,AC2}^{ah,sl}\left\{R\left(t - T_{l,AC2}^{ah,sl}\right) - R\left(t - T_{l,AC3}^{ah,sl}\right)\right\} \\ I_{l,AC}^{ah,fa}(t) &= -g_{l,AC1}^{ah,fa}\left\{R(t) - R\left(t - T_{l,AC1}^{ah,fa}\right)\right\} + g_{l,AC2}^{ah,fa}\left\{R\left(t - T_{l,AC2}^{ah,fa}\right) - R\left(t - T_{l,AC3}^{ah,fa}\right)\right\} \end{aligned} \tag{10}$$

where the subscript $l$ indicates the plasma bubble model.

For the slow-moving and fast-moving scenarios in the plasma bubble mode, $I_{GF}$ is denoted as $I_{l,GF}^{ah,sl}$ and $I_{l,GF}^{ah,fa}$, respectively. The expressions are defined with $u(t)$:

$$\begin{aligned} I_{l,GF}^{ah,fa}(t) = I_{l,GF}^{ah,sl}(t) = &-g_{l,GF1}^{ah}\left\{R\left(t - t_{l,GF}\right) - R\left(t - t_{l,GF} - T_{l,GF1}^{ah}\right)\right\} \\ &+ g_{l,GF2}^{ah}\left\{R\left(t - t_{l,GF} - T_{l,GF2}^{ah}\right) - R\left(t - t_{l,GF} - T_{l,GF3}^{ah}\right)\right\} \end{aligned} \tag{11}$$

The relevant ground parameters are calculated as follows:

$$T_{l,GF1}^{ah} = \frac{w_2}{\Delta v_l},\ T_{l,GF2}^{ah} = T_{l,GF1}^{ah} + \frac{w_b}{\Delta v_l},\ T_{l,GF3}^{ah} = T_{l,GF2}^{ah} + \frac{w_1}{\Delta v_l},\ t_{l,GF} = \frac{D}{\Delta v_l} \tag{12}$$

$$g_{l,GF1}^{ah} = g_2 \Delta v_l,\ g_{l,GF2}^{ah} = g_1 \Delta v_l \tag{13}$$

The relevant aircraft parameters are calculated as follows:

$$g_{l,AC1}^{ah,sl} = g_1(v_{AC} - \Delta v_l),\ g_{l,AC2}^{ah,sl} = g_2(v_{AC} - \Delta v_l)$$
$$g_{l,AC1}^{ah,fa} = g_2(\Delta v_l - v_{AC}),\ g_{l,AC2}^{ah,fa} = g_1(\Delta v_l - v_{AC}) \tag{14}$$

$$T_{l,AC1}^{ah,sl} = \frac{w_1}{v_{ac} - \Delta v_l},\ T_{l,AC2}^{ah,sl} = T_{l,AC1}^{ah,sl} + \frac{w_b}{v_{ac} - \Delta v_l},\ T_{l,AC3}^{ah,sl} = T_{l,AC2}^{ah,sl} + \frac{w_2}{v_{ac} - \Delta v_l}$$
$$T_{l,AC1}^{ah,fa} = \frac{w_2}{\Delta v_l - v_{ac}},\ T_{l,AC2}^{ah,fa} = T_{l,AC1}^{ah,fa} + \frac{w_b}{\Delta v_l - v_{ac}},\ T_{l,AC3}^{ah,fa} = T_{l,AC2}^{ah,fa} + \frac{w_1}{\Delta v_l - v_{ac}} \tag{15}$$

$$t_{l,LTP}^{ah,sl} = \frac{D - x + w_1 + w_b + w_2}{v_{ac}},\ t_{l,LTP}^{ah,fa} = \frac{D - x}{v_{ac}} \tag{16}$$

$I_{AC}$ and $I_{GF}$ for the plasma bubble model in the behind case are shown in Figure 7. $I_{AC}$ in the behind case, $I_{l,AC}^{be}(t)$, can be calculated from $I_{l,AC}^{ah,sl}(t)$ in Equation (10) by substituting $t$ with $t - t_{l,AC}$, because the plasma bubble starts to affect the aircraft after $t_{l,AC}$ in the behind case.

$I_{GF}$ for the plasma bubble model in the behind case, $I_{l,GF}^{be}$, can be expressed as follows:

$$I_{l,GF}^{be}(t) = -g_{l,GF1}^{be}\left\{R(t) - R\left(t - T_{l,GF1}^{be}\right)\right\} + g_{l,GF2}^{be}\left\{R\left(t - T_{l,GF2}^{be}\right) - R\left(t - T_{l,GF3}^{be}\right)\right\} \tag{17}$$

The relevant parameters are calculated as follows:

$$g_{l,GF1}^{be} = g_1 \Delta v_l,\ g_{l,GF2}^{be} = g_2 \Delta v_l \tag{18}$$

$$t_{l,LTP}^{be} = \frac{D_{air}}{v_{ac}},\ t_{l,AC} = \frac{D_{air} + x}{v_{ac} + \Delta v_l} \tag{19}$$

$$T_{l,GF1}^{be} = \frac{w_1}{\Delta v_l},\ T_{l,GF2}^{be} = T_{l,GF1}^{be} + \frac{w_b}{\Delta v_l},\ T_{l,GF3}^{be} = T_{l,GF2}^{be} + \frac{w_2}{\Delta v_l} \tag{20}$$

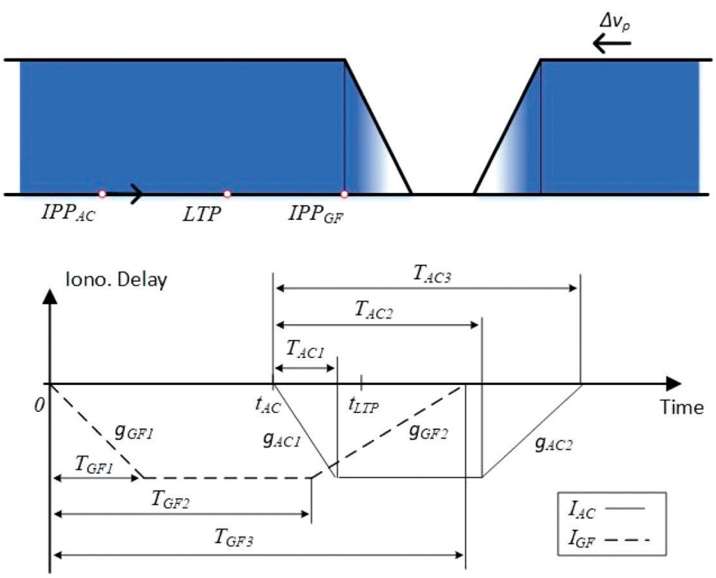


**FIGURE 7** $I_{AC}$ and $I_{GF}$ for the plasma bubble model in the behind case

## 3.2 | CSC Filter

The same CSC filter is implemented on the ground and on the aircraft to reduce the multipath and noise errors in pseudorange measurements (Hatch, 1982):

$$\hat{\rho}(t) = \omega\rho(t) + (1-\omega)\{\hat{\rho}(t-T) + \phi(t) - \phi(t-T)\} \tag{21}$$

where $\hat{\rho}$ is the smoothed pseudorange. $\omega = \tau / T$ is the filter weight with $\tau$ as the smoothing time constant, where $\tau$ is 30 s in GAST-D to reduce the time-delay effect on ionospheric errors compared with 100 s in GAST-C (Konno, 2007; RTCA DO-253D, 2017). $T$ is the sample interval, and $\rho$ and $\phi$ are the input code and carrier measurements.

If we have only $I$ in the input measurements with $\rho(t) = I(t)$, $\phi(t) = -I(t)$, the Laplace transform of the CSC filter $H(s)$ can be approximated as follows (Kim et al., 2021):

$$H(s) = \frac{\hat{I}(s)}{I(s)} \approx \frac{1-\tau s}{1+\tau s} \tag{22}$$

where $I(s)$ and $\hat{I}(s)$ represent $I(t)$ at the input and output of the CSC filter in the Laplace domain, respectively.

For the ionospheric front model in the ahead case, explicit expressions of $\hat{I}$ at the aircraft and ground under the slow-moving scenario are denoted as $\hat{I}_{m,AC}^{ah,sl}$ and $\hat{I}_{m,GF}^{ah,sl}$, respectively. Explicit expressions of $\hat{I}$ at the aircraft and ground under the fast-moving scenario are denoted as $\hat{I}_{m,AC}^{ah,fa}$ and $\hat{I}_{m,GF}^{ah,fa}$, respectively:

$$\begin{aligned}
\hat{I}_{m,AC}^{ah,sl}(t) &= L^{-1}\left\{I_{m,AC}^{ah,sl}(s)H(s)\right\} = g_{m,AC}^{ah}\left\{T_{m,AC} - \Omega\left(t, T_{m,AC}\right)\right\} \\
\hat{I}_{m,AC}^{ah,fa}(t) &= L^{-1}\left\{I_{m,AC}^{ah,fa}(s)H(s)\right\} = g_{m,AC}^{ah}\left\{\Omega\left(t,\ T_{m,AC}\right)\right\} \\
\hat{I}_{m,GF}^{ah,sl}(t) = \hat{I}_{m,GF}^{ah,fa}(t) &= L^{-1}\left\{I_{m,GF}^{ah,sl}(s)H(s)\right\} = g_{m,GF}^{ah}\left\{\Omega\left(t - t_{m,GF},\ T_{m,GF}\right)\right\}
\end{aligned} \tag{23}$$

where $I_{m,AC}^{ah,sl}(s)$, $I_{m,AC}^{ah,fa}(s)$, and $I_{m,GF}^{ah,sl}(s)$ are computed by taking the Laplace transform of $I_{m,AC}^{ah,sl}(t)$, $I_{m,AC}^{ah,fa}(t)$, and $I_{m,GF}^{ah,sl}(t)$, respectively. $L^{-1}$ indicates the inverse Laplace transform. $\Omega(t)$ is used to simplify the expression of the CCD monitor output, expressed as follows:

$$\begin{aligned}
\Omega(t, T_w) = {} & 2\tau e^{-\frac{t}{\tau}}u(t) - 2\tau u(t) + tu(t) \\
& -\{2\tau e^{-\frac{t-T_w}{\tau}}u(t-T_w) - 2\tau u(t-T_w) + (t-T_w)\ u(t-T_w)\}
\end{aligned} \tag{24}$$

In the same manner, explicit expressions of $\hat{I}$ for the aircraft and ground in the behind case, $\hat{I}_{m,AC}^{be}$ and $\hat{I}_{m,GF}^{be}$, are as follows:

$$\begin{aligned}
\hat{I}_{m,AC}^{be}(t) &= L^{-1}\left\{I_{m,AC}^{be}(s)H(s)\right\} = g_{m,AC}^{be}\left\{\Omega\left(t - t_{m,AC}, T_{m,AC}\right)\right\} \\
\hat{I}_{m,GF}^{be}(t) &= L^{-1}\left\{I_{m,GF}^{be}(s)H(s)\right\} = g_{m,GF}^{be}\left\{\Omega\left(t, T_{m,GF}\right)\right\}
\end{aligned} \tag{25}$$

Similarly, explicit expressions of $\hat{I}$ for aircraft in the plasma bubble model with the ahead case under the slow-moving and fast-moving scenarios are denoted as $\hat{I}_{l,AC}^{ah,sl}$ and $\hat{I}_{l,AC}^{ah,fa}$, respectively:

$$\begin{aligned}\hat{I}_{l,AC}^{ah,sl}(t) &= L^{-1}\left\{H(s)I_{l,AC}^{ah,sl}(s)\right\}\\ &= -g_{l,AC1}^{ah,sl}\left\{\Omega\left(t,T_{l,AC1}^{ah,sl}\right)\right\}+g_{l,AC2}^{ah,sl}\left\{\Omega\left(t-T_{l,AC2}^{ah,sl},T_{l,AC3}^{ah,sl}-T_{l,AC2}^{ah,sl}\right)\right\}\\ \hat{I}_{l,AC}^{ah,fa}(t) &= L^{-1}\left\{H(s)I_{l,AC}^{ah,fa}(s)\right\}\\ &= -g_{l,AC1}^{ah,fa}\left\{\Omega\left(t,T_{l,AC1}^{ah,fa}\right)\right\}+g_{l,AC2}^{ah,fa}\left\{\Omega\left(t-T_{l,AC2}^{ah,fa},T_{l,AC3}^{ah,fa}-T_{l,AC2}^{ah,fa}\right)\right\}\end{aligned} \tag{26}$$

where $I_{l,AC}^{ah,sl}(s)$ and $I_{l,AC}^{ah,sl}(s)$ are obtained by taking the Laplace transform of $I_{l,AC}^{ah,sl}(t)$ and $I_{l,AC}^{ah,sl}(t)$, respectively.

Explicit expressions of $\hat{I}$ for the ground in the plasma bubble model with the ahead case under the slow-moving and fast-moving scenarios are denoted as $\hat{I}_{l,GF}^{ah,sl}$ and $\hat{I}_{l,GF}^{ah,fa}$, respectively:

$$\begin{aligned}\hat{I}_{l,GF}^{ah,fa}(t) = \hat{I}_{l,GF}^{ah,sl}(t) &= L^{-1}\left\{H(s)I_{l,GF}^{ah,fa}(s)\right\}\\ &= -g_{l,GF1}^{ah}\left\{\Omega\left(t-t_{l,GF},T_{l,GF1}^{ah}\right)\right\}+g_{l,GF2}^{ah}\left\{\Omega\left(t-t_{l,GF}-T_{l,GF2}^{ah},T_{l,GF3}^{ah}-T_{l,GF2}^{ah}\right)\right\}\end{aligned} \tag{27}$$

where $I_{l,GF}^{ah,fa}(s)$ is obtained by taking the Laplace transform of $I_{l,GF}^{ah,fa}(t)$.

In the behind case, $\hat{I}$ on the ground for the plasma bubble model, $\hat{I}_{l,GF}^{be}(t)$, can be expressed as follows:

$$\begin{aligned}\hat{I}_{l,GF}^{be}(t) &= L^{-1}\left\{H(s)I_{l,GF}^{be}(s)\right\}\\ &= -g_{l,GF1}^{be}\left\{\Omega\left(t,T_{l,GF1}^{be}\right)\right\}+g_{l,GF2}^{be}\left\{\Omega\left(t-T_{l,GF2}^{be},T_{l,GF3}^{be}-T_{l,GF2}^{be}\right)\right\}\end{aligned} \tag{28}$$

where $I_{l,GF}^{be}(s)$ is obtained by taking the Laplace transform of $I_{l,GF}^{be}(t)$. $\hat{I}$ for the aircraft in the behind case under the plasma bubble model, $\hat{I}_{l,AC}^{be}(t)$, can be computed from $\hat{I}_{l,AC}^{ah,sl}(t)$ by substituting $t$ with $t-t_{l,AC}$, because the plasma bubble starts to affect the aircraft after $t_{l,AC}$ in the behind case.

## 4 | IONOSPHERIC MONITORS

In GAST-D, a CCD monitor, DSIGMA monitor, and IGM are implemented for ionosphere monitoring. Compared with GAST-C, in which only a CCD monitor is installed on the ground, the overall performance in GAST-D is improved by monitoring ionospheric anomalies at both the ground and aircraft. Explicit expressions for these monitors are given as follows.

### 4.1 | CCD Monitor

The CCD monitor implemented on the ground consists of a second-order cascaded filter to detect the ionospheric gradient (Simili & Pervan, 2006). In the Laplace domain, the output of the CCD monitor, $Out_{ccd}$, can be expressed as follows (Kim et al., 2021):

$$Out_{ccd}(s) = \frac{2sI(s)}{(\tau_{ccd}s+1)^2} \tag{29}$$

where $\tau_{ccd}$ is the filter time constant of the CCD monitor, which is set as 25 s (Pullen et al., 2017). $I(s)$ is the Laplace form of $I_{GF}$, with $I_{m,GF}(s)$ denoted for the ionospheric front model and $I_{l,GF}(s)$ for the plasma bubble model.

By substituting $I_{m,GF}^{ah,sl}(s)$ or $I_{m,GF}^{ah,fa}(s)$ for $I(s)$ in Equation (29), $Out_{ccd}$ for the ionospheric front model in the ahead case, $Out_{m,ccd}^{ah}$, can be explicitly expressed as follows:

$$Out_{m,ccd}^{ah}(t) = L^{-1}\left\{\frac{2sI_{m,GF}^{ah,sl}(s)}{(\tau s+1)^2}\right\} = 2g_{m,GF}^{ah}\left\{\Psi\left(t-t_{m,GF}\right)-\Psi\left(t-t_{m,GF}-T_{m,GF}\right)\right\} \quad (30)$$

where $\Psi(t)$ is used to simplify the expression:

$$\Psi(t) = \left(1-\frac{t+\tau_{ccd}}{\tau_{ccd}}e^{\frac{-t}{\tau_{ccd}}}\right)u(t) \quad (31)$$

$Out_{ccd}$ for the behind case with the ionospheric front model, $Out_{m,ccd}^{be}(t)$, can be computed as follows:

$$Out_{m,ccd}^{be}(t) = L^{-1}\left\{\frac{2sI_{m,GF}^{be}(s)}{(\tau s+1)^2}\right\} = 2g_{m,GF}^{be}\left\{\Psi(t)-\Psi\left(t-T_{m,GF}\right)\right\} \quad (32)$$

$Out_{ccd}$ for the plasma bubble model in the ahead case, $Out_{l,ccd}^{ah}$, is obtained by substituting $I_{l,GF}^{ah,sl}(s)$ or $I_{l,GF}^{ah,fa}(s)$ for $I(s)$ in Equation (29):

$$\begin{aligned} Out_{l,ccd}^{ah}(t) = L^{-1}\left\{\frac{2sI_{l,GF}^{ah,sl}(s)}{(\tau s+1)^2}\right\} &= 2g_{l,GF1}^{ah}\left\{\Psi\left(t-t_{l,GF}\right)-\Psi\left(t-t_{l,GF}-T_{l,GF1}^{ah}\right)\right\} \\ &\quad -2g_{l,GF2}^{ah}\left\{\Psi\left(t-t_{l,GF}-T_{l,GF2}^{ah}\right)-\Psi\left(t-t_{l,GF}-T_{l,GF3}^{ah}\right)\right\} \end{aligned} \quad (33)$$

Similarly, $Out_{ccd}$ for the plasma bubble model in the behind case, $Out_{l,ccd}^{be}$, can be computed by substituting $I_{l,GF}^{be}(s)$ into Equation (29):

$$\begin{aligned} Out_{l,ccd}^{be}(t) &= L^{-1}\left\{\frac{2sI_{l,GF}^{be}(s)}{(\tau s+1)^2}\right\} \\ &= 2g_{l,GF1}^{be}\left\{\Psi(t)-\Psi\left(t-T_{l,GF1}^{be}\right)\right\}-2g_{l,GF2}^{be}\left\{\Psi\left(t-T_{l,GF2}^{be}\right)-\Psi\left(t-T_{l,GF3}^{be}\right)\right\} \end{aligned} \quad (34)$$

The minimum detectable divergence rate of the CCD $(\mathrm{MDDR}_{\mathrm{ccd}})$ is computed based on the probability of a false alarm (PFA), probability of missed detection (PMD), and standard deviation of test statistics (Pullen et al., 2017):

$$\mathrm{MDDR}_{\mathrm{ccd}} = (K_{ffd}+K_{md})\sigma_{ccd} = 85.18\,mm/s \quad (35)$$

where $\sigma_{ccd}$ is the standard deviation of test statistics, $K_{ffd}$ is the K-factor for a given PFA, and $K_{md}$ is the K-factor for a given PMD. The values are set as follows: $\sigma_{ccd}$ is bounded as 6.9 mm/s, $K_{ffd}$ is 5.91, and $K_{md}$ is 6.0 (Pullen et al., 2017). Because the simulation only involves deterministic parameters, the derived CCD monitor outputs are theoretical and free of noise. Meanwhile, the $\mathrm{MDDR}_{\mathrm{ccd}}$ value is compared with the CCD monitor outputs.

The $Out_{m,ccd}^{ah}$ and $Out_{l,ccd}^{ah}$ results for different $\Delta v_m$ and $\Delta v_l$ values under the ionospheric front model and plasma bubble model in the ahead case are shown

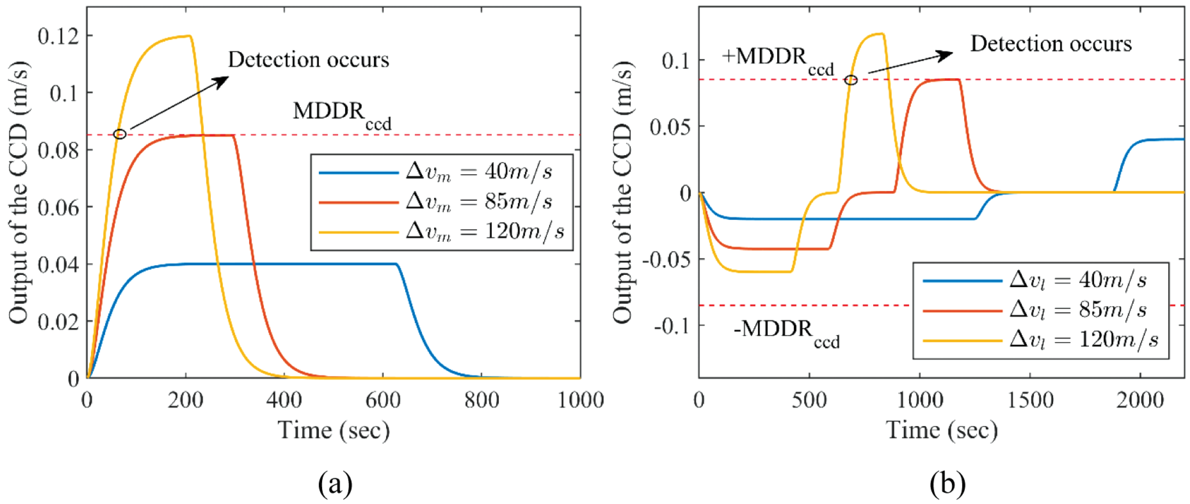


**FIGURE 8** Simulation of the CCD monitor output (a) Ionospheric front model (b) Plasma bubble model

in Figure 8. The simulation results for the ionospheric front model were obtained for $g = 500$ mm/km and $w = 25$ km. For the plasma bubble model, $g_1 = 500$ mm/km, $w_1 = 25$ km, $g_2 = 250$ mm/km, $w_2 = 50$ km, and $w_b = 25$ km. Detection occurs when $Out^{ah}_{m,ccd}$ or $Out^{ah}_{l,ccd}$ exceeds $\mathrm{MDDR}_{ccd}$, as indicated by the black ellipse.

As shown in Figure 8, the CCD monitor cannot detect an ionospheric front when $\Delta v_m$ is less than 85 m/s with $g = 500$ mm/km. Moreover, the CCD monitor cannot detect a plasma bubble when $\Delta v_l$ is less than 85 m/s with $g_1 = 500$ mm/km and $g_2 = 250$ mm/km. For the plasma bubble model, two peaks with opposite signs are observed due to the presence of double slopes in the plasma bubble model. The absolute value of the peak is determined by $g_1$ and $g_2$. Moreover, $Out^{ah}_{m,ccd}$ and $Out^{ah}_{l,ccd}$ are larger with earlier detection when $\Delta v_m$ and $\Delta v_l$ are larger. However, the time period during which the CCD monitor is affected by the ionospheric front or plasma bubble tends to be shorter when $\Delta v_m$ or $\Delta v_l$ is larger.

## 4.2 | DSIGMA

On an aircraft, DSIGMA monitors the difference between two CSC filter outputs with different time constants:

$$Out_{dsigma} = \hat{I}^{\tau_2}_{AC} - \hat{I}^{\tau_1}_{AC} \tag{36}$$

where the superscripts $\tau_2$ and $\tau_1$ represent two time constants, i.e., 100 s and 30 s, respectively. For the ionospheric front model, $Out_{dsigma}$ for the slow-moving and fast-moving scenarios in the ahead case, $Out^{ah,sl}_{m,dsigma}$ and $Out^{ah,fa}_{m,dsigma}$, can be explicitly expressed by substituting $\hat{I}^{ah,fa}_{m,AC}(t)$ and $\hat{I}^{ah,sl}_{m,AC}(t)$ in Equation (33):

$$Out^{ah,fa}_{m,dsigma}(t) = -Out^{ah,sl}_{m,dsigma}(t) = g^{ah}_{m,AC}\left(\Theta(t) - \Theta\left(t - T_{m,AC}\right)\right) \tag{37}$$

where $\Theta(t)$ is expressed as follows:

$$\Theta(t) = 2\left\{\tau_2 e^{\frac{-t}{\tau_2}} - \tau_1 e^{\frac{-t}{\tau_1}} - (\tau_2 - \tau_1)\right\}u(t) \tag{38}$$

By substituting $\hat{I}^{be}_{m,AC}(t)$ in Equation (33), $Out_{dsigma}$ for the ionospheric front model in the behind case, $Out^{be}_{m,dsigma}$, can be computed as follows:

$$Out^{be}_{m,dsigma}(t) = g^{be}_{m,AC}\left(\Theta\left(t - t_{m,AC}\right) - \Theta\left(t - t_{m,AC} - T_{m,AC}\right)\right) \tag{39}$$

Similarly, $Out_{dsigma}$ in the ahead case for the slow-moving and fast-moving scenarios in the plasma bubble model are denoted as $Out^{ah,sl}_{l,dsigma}$ and $Out^{ah,fa}_{l,dsigma}$, respectively. The expressions are obtained by substituting $\hat{I}^{ah,fa}_{l,AC}(t)$ and $\hat{I}^{ah,sl}_{l,AC}(t)$ into Equation (33):

$$\begin{aligned} Out^{ah,sl}_{l,dsigma}(t) &= g^{ah,sl}_{l,AC2}\left(\Theta\left(t - T^{ah,sl}_{l,AC2}\right) - \Theta\left(t - T^{ah,sl}_{l,AC3}\right)\right) - g^{ah,sl}_{l,AC1}\left(\Theta(t) - \Theta\left(t - T^{ah,sl}_{l,AC1}\right)\right) \\ Out^{ah,fa}_{l,dsigma}(t) &= g^{ah,fa}_{l,AC2}\left(\Theta\left(t - T^{ah,fa}_{l,AC2}\right) - \Theta\left(t - T^{ah,fa}_{l,AC3}\right)\right) - g^{ah,fa}_{l,AC1}\left(\Theta(t) - \Theta\left(t - T^{ah,fa}_{l,AC1}\right)\right) \end{aligned} \tag{40}$$

$Out_{dsigma}$ for the plasma bubble model in the behind case, $Out^{be}_{l,dsigma}$, can also be expressed by $Out^{ah,sl}_{l,dsigma}(t)$ with $t$ substituted by $t - t_{l,AC}$.

The minimum detectable error (MDE) of DSIGMA ($MDE_{dsigma}$) is computed from PFA, PMD, and the standard deviation of test statistics (Pullen et al., 2017):

$$MDE_{dsigma} = \left(K_{ffd} + K_{md}\right)\sigma_{dsigma} = 2.02\,m \tag{41}$$

where $\sigma_{dsigma}$ is the standard deviation of test statistics. The values of $K_{ffd}$, $K_{md}$, and $\sigma_{dsigma}$ are set as follows: $\sigma_{dsigma}$ is bounded as 0.714 m, $K_{ffd}$ is 5.61, and $K_{md}$ is 6.0 (Pullen et al., 2017).

The output of DSIGMA for different $\Delta v_m$ or $\Delta v_l$ values in the ahead case is shown in Figure 9. The simulation results for the ionospheric front model were obtained for $g = 500$ mm/km and $w = 25$ km. The simulation results for the plasma bubble model were obtained for $g_1 = 500$ mm/km, $g_2 = 250$ mm/km, $w_1 = 25$ km, $w_2 = 50$ km, and $w_b = 25$ km. Detection occurs when the output of DSIGMA exceeds $\mathrm{MDE}_{\mathrm{dsigma}}$, as indicated by the black ellipses.

As shown in Figure 9, the DSIGMA monitor cannot detect an ionospheric front when $\Delta v_m$ is between 42 m/s and 98 m/s with $g = 500$ mm/km. Moreover,

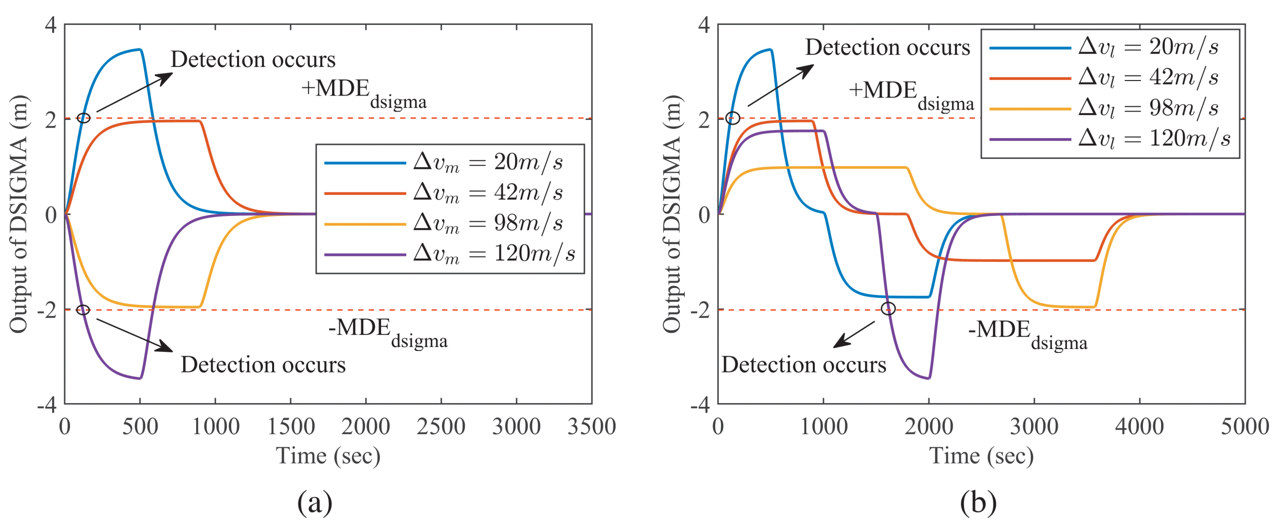


**FIGURE 9** Simulation results for the DSIGMA output (a) Ionospheric front model (b) Plasma bubble model

the DSIGMA monitor cannot detect a plasma bubble when $\Delta v_l$ is between 42 m/s and 98 m/s with $g_1 = 500\,mm/km$ and $g_2 = 250\,mm/km$. Two peaks with opposite signs are observed because of the presence of double slopes in the plasma bubble model. The absolute value of the peak is determined by $g_1$ and $g_2$. Moreover, a larger speed difference between $\Delta v_m$ and $v_{ac}$ results in a larger $Out_{m,dsigma}^{ah}$, whereas the period during which the DSIGMA monitor is affected by the ionospheric front tends to be shorter. Similarly, a larger difference between $\Delta v_l$ and $v_{ac}$ results in a larger $Out_{l,dsigma}^{ah}$, whereas the period during which the DSIGMA monitor is affected by the plasma bubble tends to be shorter.

### 4.3 | IGM

An IGM on the ground directly monitors the ionospheric gradient among multiple ground stations by using double-difference carrier phase measurements, where the baselines are on the order of several hundred meters (Khanafseh et al., 2012).

For the ionospheric front model, the IGM outputs in both the ahead and behind cases, $Out_{m,igm}^{ah}$ and $Out_{m,igm}^{be}$, are the gradient magnitudes when the ground is affected by an anomaly:

$$\begin{aligned} Out_{m,igm}^{ah}(t) &= g\left\{u\left(t - t_{m,GF}\right) - u\left(t - t_{m,GF} - T_{m,GF}\right)\right\} \\ Out_{m,igm}^{be}(t) &= g\left\{u\left(t\right) - u\left(t - T_{m,GF}\right)\right\} \end{aligned} \tag{42}$$

For the plasma bubble model, the IGM outputs in the ahead and behind cases are denoted as $Out_{l,igm}^{ah}$ and $Out_{l,igm}^{be}$, respectively:

$$\begin{aligned} Out_{l,igm}^{ah}(t) = g_2 &\left\{u\left(t - t_{l,GF}\right) - u\left(t - t_{l,GF} - T_{l,GF1}^{ah}\right)\right\} + \\ & g_1\left\{u\left(t - t_{l,GF} - T_{l,GF1}^{ah} - T_{l,GF2}^{ah}\right) - u\left(t - t_{l,GF} - T_{l,GF1}^{ah} - T_{l,GF2}^{ah} - T_{l,GF3}^{ah}\right)\right\} \\ Out_{l,igm}^{be}(t) = g_1 &\left\{u(t) - u\left(t - T_{l,GF1}^{be}\right)\right\} + \\ & g_2\left\{u\left(t - T_{l,GF1}^{be} - T_{l,GF2}^{be}\right) - u\left(t - T_{l,GF1}^{be} - T_{l,GF2}^{be} - T_{l,GF3}^{be}\right)\right\} \end{aligned} \tag{43}$$

The minimum detectable gradient (MDG) of the IGM ($MDG_{igm}$) for the IGM proposed by Khanafseh et al. (2012) is computed from the PFA, PMD, and standard deviation of test statistics (Pullen et al., 2017):

$$MDG_{igm} = K_{ffd}\sigma_{igm,co} + K_{md}\sigma_{igm,in} = 250\,mm/km \tag{44}$$

where $\sigma_{igm,co}$ and $\sigma_{igm,in}$ are continuity and integrity standard deviations of the IGM, respectively. The values of $\sigma_{igm,co}$, $\sigma_{igm,in}$, $K_{ffd}$, and $K_{md}$ are set as follows: $\sigma_{igm,co}$ and $\sigma_{igm,in}$ are bounded as 16.7 mm/km and 26.3 mm/km, respectively, $K_{ffd}$ is 5.91, and $K_{md}$ is 6.0 (Pullen et al., 2017).

The $Out_{m,igm}^{ah}$ results for different $\Delta v_m$ and $g$ values in the ionospheric front model and $Out_{l,igm}^{ah}$ results for different $\Delta v_l$, $g_1$, and $g_2$ values in the plasma bubble model are shown in Figure 10. The simulation results for the ionospheric front model were obtained for $w = 25\,km$ and $D = 10\,km$. The simulation results for the plasma bubble model were obtained for $w_1 = 25\,km$, $w_2 = 50\,km$, $w_b = 25\,km$, and $D = 10\,km$. Detection occurs when $Out_{m,igm}^{ah}$ or $Out_{l,igm}^{ah}$ exceeds $MDG_{igm}$, as indicated by the black ellipse.

As shown in Figure 10, $Out^{ah}_{m,igm}$ is larger when $g$ is larger, and $Out^{ah}_{l,igm}$ is larger when $g_1$ is larger. For a larger $\Delta v_m$ or $\Delta v_l$, detection occurs earlier, but the period during which the IGM is affected by the ionospheric front or plasma bubble tends to be shorter.

## 5 | CLOSED-FORM ANALYSIS OF UNDETECTED DIFFERENTIAL RANGE ERRORS

In this section, a closed-form expression for the largest ionosphere-induced $Er_{undetected}$ ($Er^{max}_{undetected}$) is derived as a function of threat parameters of ionospheric speed and gradient magnitude, i.e., $\Delta v_m$ and $g$ for the ionospheric front model and $\Delta v_l$, $g_1$, and $g_2$ for the plasma bubble model. Therefore, an exhaustive simulation must be conducted to search for $Er^{max}_{undetected}$ among other parameters, e.g., $w$ and $D$.

The parameter ranges for the ionospheric front model and plasma bubble model (shown in Tables 2 and 3) are defined similarly to those for GAST-C

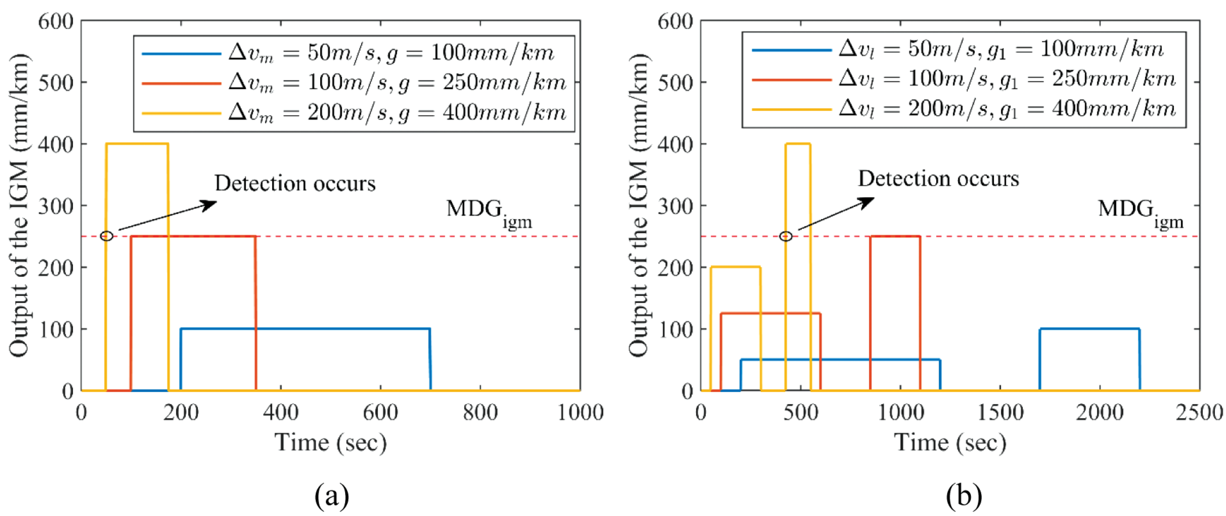


**FIGURE 10** Simulation results of the IGM output (a) Ionospheric front model (b) Plasma bubble model

**TABLE 2**
Range of Plasma Bubble Threat Model Parameters for Simulation (Lee et al., 2017; Saito et al., 2017)

| Threat parameter | Range | Step |
|---|---|---|
| $g_1$ | 200–500 (mm/km) | 5 (mm/km) |
| $g_2$ | 200–500 (mm/km) | 5 (mm/km) |
| $w_1$ | 25–200 (km) | 25 (km) |
| $w_b$ | 25–200 (km) | 25 (km) |
| $w_2$ | $g_1 * w_1 / g_2$ | NA |
| $\Delta v_l$ | 0–500 (m/s) | 1 (m/s) |
| $D(D_{air})$ | 0–$D^u$ (km) | 0.25 (km) |
| $D_{air}$ | 0–$D^u$ (km) | 0.25 (km) |

**TABLE 3**
Range of Ionospheric Front Threat Model Parameters for Simulation (Kim et al., 2017)

| Threat parameter | Range | Step |
|---|---|---|
| $g$ | 200–500 (mm/km) | 5 (mm/km) |
| $\Delta v_m$ | 0–500 (m/s) | 1 (m/s) |
| $w$ | 25–200 (km) | 25 (km) |
| $D$ | 0–$D^u$ (km) | 0.25 (km) |
| $D_{air}$ | 0–$D^u$ (km) | 0.25 (km) |

(Kim et al., 2017; Lee et al., 2017; Saito et al., 2017). The upper limit of $D$ is generated as follows:

$$D^u = max\{200km, D_{max}\} \tag{45}$$

Normally, 200 km is sufficient to generate $Er^{max}_{undetected}$. $D_{max}$ for the ionospheric front model is denoted as $D_{m,max}$, which is needed only when $\Delta v_m$ is close to $v_{AC}$:

$$D_{m,max} = \frac{(w-x)\Delta v_m}{|v_{AC} - \Delta v_m|} \tag{46}$$

$D_{max}$ for the plasma bubble model is denoted as $D_{l,max}$, which is needed when $\Delta v_l$ is close to $v_{AC}$ :

$$D_{l,max} = \frac{(w_1 + w_b + w_2 - x)\Delta v_l}{|v_{AC} - \Delta v_l|} \tag{47}$$

For each simulation round with a particular set of threat parameters, $Er$ is calculated only when the aircraft arrives at the LTP to reduce the computation load. The maximum outputs of the CCD monitor ($Out^{max}_{ccd}$), DSIGMA monitor ($Out^{max}_{dsigma}$), and IGM ($Out^{max}_{igm}$) during the simulation are used because there are multiple opportunities to detect the ionospheric anomaly (Pullen et al., 2017). $Er_{undetected}$ is recorded when $Out^{max}_{ccd}$ is smaller than $\mathrm{MDDR}_{ccd}$, $Out^{max}_{dsigma}$ is smaller than $\mathrm{MDE}_{dsigma}$, and $Out^{max}_{igm}$ is smaller than $\mathrm{MDG}_{igm}$.

For a given $w$, $\Delta v_m$, and $g$ for the ionospheric front model in the ahead case, $Er^{max}_{undetected}$ can be obtained by searching for the maximum $Er_{undetected}$ across all possible values of $D$:

$$\begin{aligned} Er^{max}_{undetected} = \max\{&Er_{undetected}(D) \mid D \in Out^{max}_{dsigma}(D) < \mathrm{MDE}_{dsigma} \\ &\cap Out^{max}_{ccd}(D) < \mathrm{MDDR}_{ccd} \cap Out^{max}_{igm}(D) < \mathrm{MDG}_{igm}\} \end{aligned} \tag{48}$$

For the ionospheric front model in the behind case, $Er^{max}_{undetected}$ can be obtained by substituting $D_{air}$ for $D$ in Equation (42). For the plasma bubble model, $Er^{max}_{undetected}$ can be obtained in the same way. When $Out^{max}_{dsigma}$, $Out^{max}_{ccd}$, and $Out^{max}_{igm}$ are computed, the recovery procedure should be considered. As an example, Figure 11 illustrates the recovery procedure for the CCD monitor.

As shown in Figure 11, recovery occurs when $Out_{ccd}$ remains below the re-admittance level of the CCD monitor ($Tre_{ccd}$) for a certain period ($B_{delay}$). The CCD monitor and $Out^{max}_{ccd}$ are reset at the time of recovery. The parameters for each ionospheric monitor related to the recovery procedure are listed in Table 4.

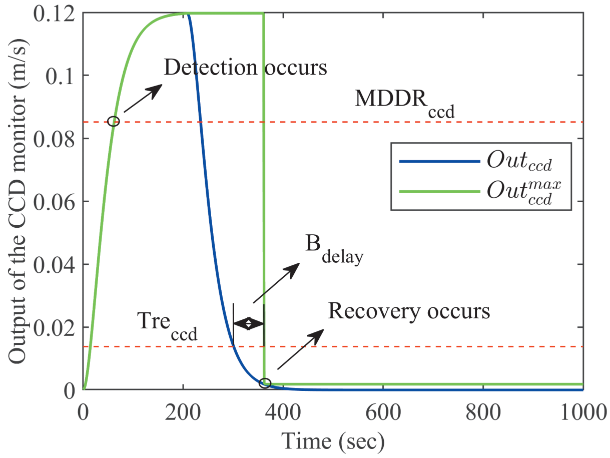


**FIGURE 11** Recovery procedure for the CCD monitor

**TABLE 4**
Recovery Procedure Parameters

| Ionospheric monitor | MDE/MDDR/MDG | Tre | $B_{delay}$ |
|---|---|---|---|
| DSIGMA | 2.02 (m) | 0.348 (m) | 60 (s) |
| CCD | 0.085 (m/s) | 0.0138 (m/s) | 60 (s) |
| IGM | 250 (mm/km) | 33.4 (mm/km) | 60 (s) |

Taking the ahead case of the ionospheric front model as an example, the determination of $Er_{undetected}^{max}$ across all possible $D$ values is shown in Figure 12. The results were obtained for $g = 500$ mm/km and $w = 25$ km. $\Delta v_m$ is set as 40 m/s and 120 m/s for the slow-moving and fast-moving scenarios, respectively. $Er_{undetected}^{max}$ is found by searching for the maximum $Er$ within the range of $D$ for which no detection occurs before $t_{LTP}$ for all ionospheric monitors.

$Er_{undetected}^{max}$ can be obtained by exhaustive offline simulations, as shown above. Based on the simulation results, a linear closed-form expression is developed to bound the results as an analytical way to represent the results. Although a polynomial expression can bound $Er_{undetected}^{max}$ more tightly, a simplified, conservative linear expression is used.

$Er_{undetected}^{max}$ for the ionospheric front model is shown in Figure 13. The results are divided into two parts: severe gradients with gradient magnitudes larger than or equal to 250 mm/km and moderate gradients with gradient magnitudes smaller than 250 mm/km. The results for different gradient values are shown by different colors.

In Figure 13, only the ahead case is presented for the severe gradient condition, while both the ahead case and the behind case are presented for the moderate gradient condition. This difference is due to the fact that the geometric model in the behind case assumes that $IPP_{GF}$ occurs at the rear edge of the ionospheric front model, which would be detected by the IGM when the simulation begins. When $\Delta v_m$ is small, the CCD monitor is unable to detect an ionospheric front. However, because of the presence of the DSIGMA monitor and the IGM, the ionospheric front can be detected before the aircraft arrives at the LTP with no $Er_{undetected}$ generated. For a larger $\Delta v_m$, $Er_{undetected}^{max}$ reaches a maximum because all ionospheric monitors fail to detect the ionospheric front before the aircraft arrives at the LTP. As $\Delta v_m$ becomes larger, $Er_{undetected}^{max}$ starts to decrease because the ionospheric front is observed by the ionospheric monitors before $Er_{undetected}^{max}$ reaches a maximum.

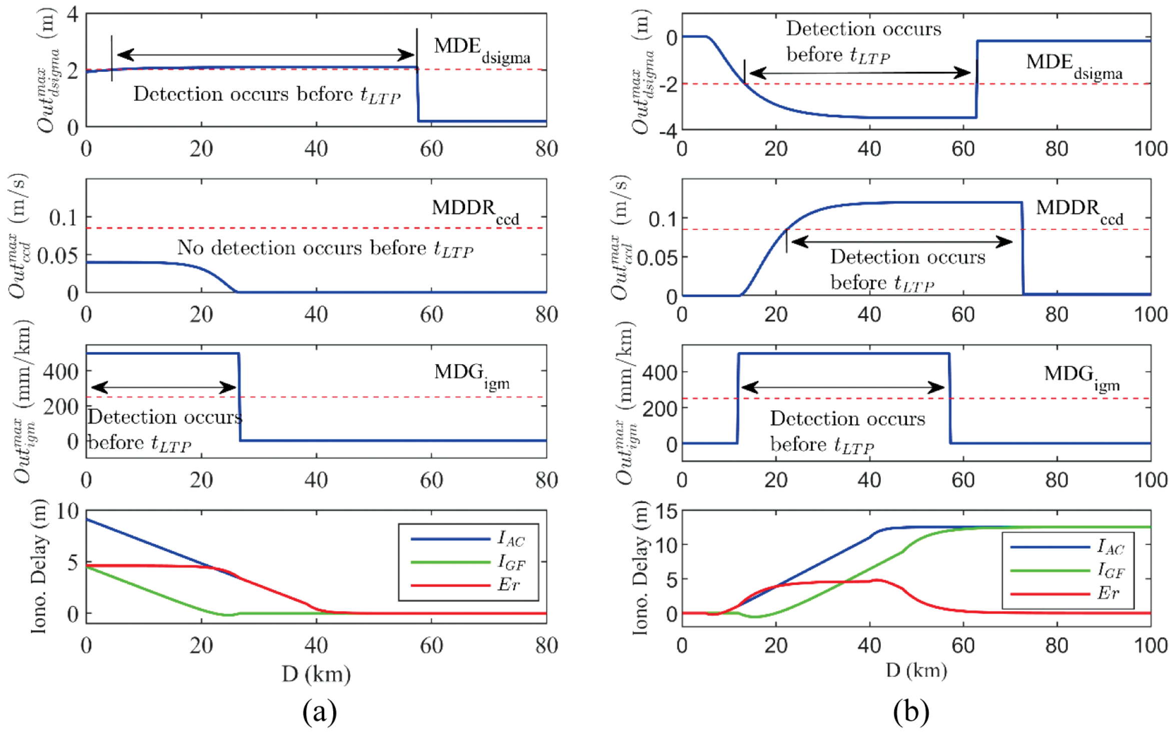


**FIGURE 12** $Er_{undetected}^{max}$ for the ionospheric front model, given g=500 mm/km and $w$=25 km (a) Slow-moving scenario for the ahead case, $\Delta v_m = 40\,m/s$ (b) Fast-moving scenario for the ahead case, $\Delta v_m = 120\,m/s$

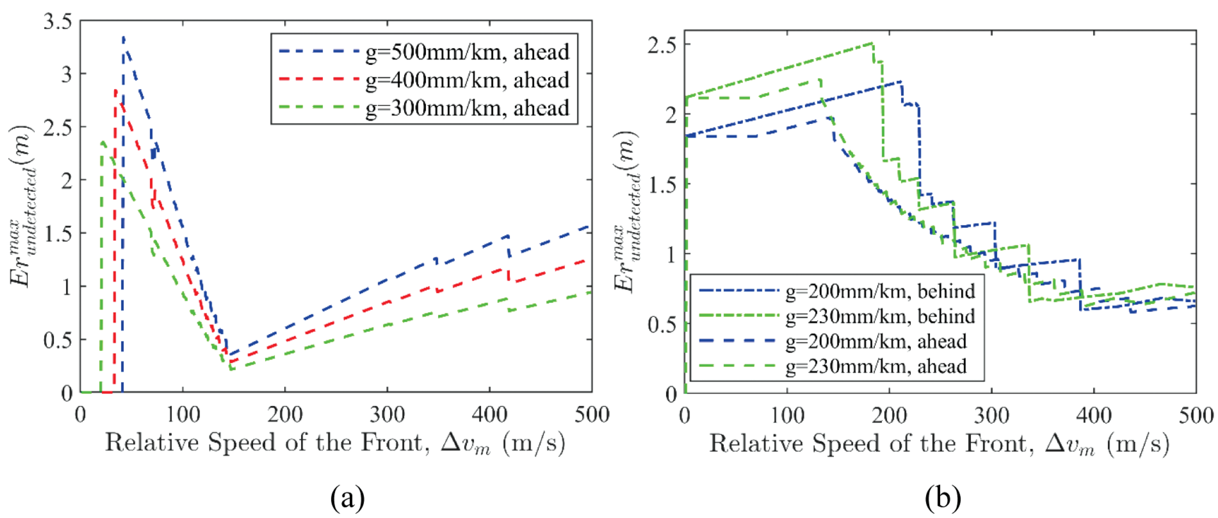


**FIGURE 13** Exhaustive simulation results of the largest undetected differential range errors induced by an ionospheric front (a) Ionospheric front model with severe gradients (b) Ionospheric front model with moderate gradients

When $\Delta v_m$ is sufficiently large, $Er_{undetected}^{max}$ converges to a value proportional to the gradient magnitude. For the moderate gradient condition, both the behind case and ahead case must be considered. In addition, $Er_{undetected}^{max}$ for the behind case is larger than that of the ahead case because the ionospheric front affects the ground earlier than the aircraft and cannot be detected by the ground IGM. $Er_{undetected}^{max}$ continues increasing as $\Delta v_m$ increases until the ionospheric front can be detected by the DSIGMA monitor.

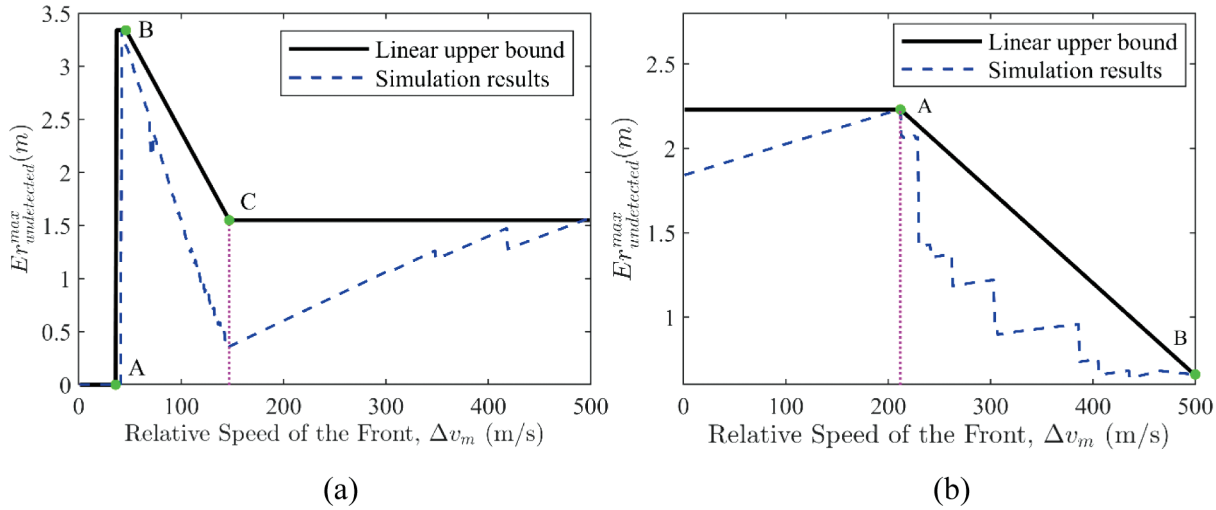


**FIGURE 14** Example of the linear bound as a function of $\Delta v_m$ and $g$ of the ionospheric front model (a) Ionospheric front model with a severe gradient (b) Ionospheric front model with a moderate gradient

The linear expression of $Er^{max}_{undetected}$ for the ionospheric front model is divided into two parts: severe gradients with $g \geq 250$ mm/km and moderate gradients with $g < 250$ mm/km, as shown in Figure 14. The blue dashed line represents exhaustive simulation results with $g = 500$ mm/km and $g = 200$ mm/km for severe gradients and moderate gradients, respectively. The black solid line indicates the linear expression as a function of $\Delta v_m$ and $g$.

As shown in Figure 14, three transition points, namely A, B, and C, are defined to bound $Er^{max}_{undetected}$ under a severe gradient. Point A is used to indicate $\Delta v_m$ when the ionospheric front is fully mitigated without $Er^{max}_{undetected}$ generated. In contrast, point B indicates the maximum $Er^{max}_{undetected}$. The upper bound of $Er^{max}_{undetected}$ between point A and point B is conservatively set as the maximum $Er^{max}_{undetected}$. The x-coordinate of point C denotes the $\Delta v_m$ value when $Er^{max}_{undetected}$ is the smallest, and the y-coordinate of point C indicates the converged $Er^{max}_{undetected}$ value when $\Delta v_m$ is close to 500 m/s. To obtain a linear expression of $Er^{max}_{undetected}$, it is necessary to define the expressions of points A, B, and C as a function of $\Delta v_m$ and $g$. $A^{se}_{\Delta v_m}$, $B^{se}_{\Delta v_m}$, and $C^{se}_{\Delta v_m}$ are used to denote the $\Delta v_m$ values at points A, B, and C, respectively, where the superscript *se* indicates the severe gradient condition. The $Er^{max}_{undetected}$ values for points B and C are represented by $B^{se}_{m,Er}$ and $C^{se}_{m,Er}$, respectively.

$A^{se}_{\Delta v_m}$ and $B^{se}_{\Delta v_m}$ as a function of $g$ (mm/km) are shown in Figure 15, indicated by blue and black lines, respectively. The red dots represent the simulated results of $\Delta v_m$ when $Er^{max}_{undetected}$ reaches the maximum value. For a given $g$, the speed difference between $v_{AC}$ and $\Delta v_m$ for the red dots can be approximately calculated from $\mathrm{MDE}_{dsigma}$, $\tau_1$, and $\tau_2$.

$$\Delta v_m - v_{AC} \approx \frac{\mathrm{MDE}_{dsigma}}{2g(\tau_2 - \tau_1)} \tag{49}$$

Then, $A^{se}_{\Delta v_m}$ and $B^{se}_{\Delta v_m}$ can be derived analytically as the upper and lower limits of the red dots:

$$A^{se}_{\Delta v_m} = v_{AC} - \frac{\mathrm{MDE}_{dsigma}}{2g(\tau_2 - \tau_1)} - 5,\ B^{se}_{\Delta v_m} = v_{AC} - \frac{\mathrm{MDE}_{dsigma}}{2g(\tau_2 - \tau_1)} + 3 \tag{50}$$

$C_{\Delta v_m}^{se}$ is obtained when the physical separation of the ground IPP and aircraft IPP is equal to zero:

$$x+2\tau\left(v_{AC}-C_{\Delta v_m}^{se}\right)=0 \tag{51}$$

$B_{m,Er}^{se}$ and $C_{m,Er}^{se}$ are determined by a fitting method, as shown in Figure 16. The red stars in the top and bottom figures show the simulated results of the maximum and converged $Er_{undetected}^{max}$. The black line represents the fitted result expressed as a function of $g$:

$$B_{m,Er}^{se}=0.0049g+0.8874,\ C_{m,Er}^{se}=0.00314g \tag{52}$$

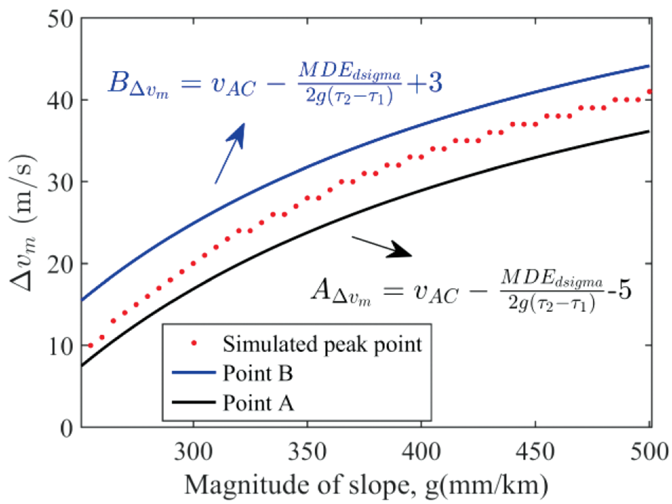


**FIGURE 15** Determination of $\Delta v_m$ for points A and B

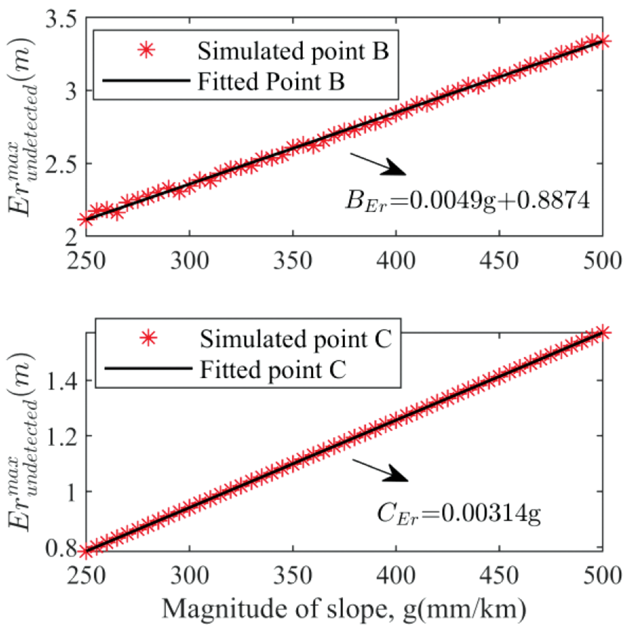


**FIGURE 16** Determination of $Er_{undetected}^{max}$ for points B and C

With points A, B, and C determined, the linear closed-form expression for $Er_{undetected}^{max}$ in the ionospheric front model with a severe gradient can be expressed as follows:

$$Er_{undetected}^{max}(\Delta v_m)=\begin{cases}0 & 0<\Delta v_m \le A_{\Delta v_m}^{se} \\ B_{m,Er}^{se} & A_{\Delta v_m}^{se}<\Delta v_m \le B_{\Delta v_m}^{se} \\ Er^{de}\left(\Delta v_m, B_{\Delta v_m}^{se}, C_{\Delta v_m}^{se}, B_{m,Er}^{se}, C_{m,Er}^{se}\right) & B_{\Delta v_m}^{se}<\Delta v_m \le C_{\Delta v_m}^{se} \\ C_{m,\Delta Er}^{se} & C_{\Delta v_m}^{se}<\Delta v_m \le 500\end{cases} \tag{53}$$

where $Er^{de}$ is a decreasing linear function:

$$Er^{de}(\Delta v, X_1, X_2, Y_1, Y_2)=Y_1-\frac{Y_2-Y_1}{X_1-X_2}(\Delta v-X_1) \tag{54}$$

The established linear expression has the advantage that the structure remains the same if we vary the aircraft speed as input. In other words, the parameters of the expression can be adjusted based on the input aircraft speed with no need to define a new expression. To demonstrate this feature, we used a $v_{AC}$ of 82.8 m/s as an example; this value is the aircraft speed at the LTP, as defined in a previously reported speed profile (ICAO, 2018). The simulation results and linear expression are shown in Figure 17.

As shown in Figure 17, the linear expression can still bound the simulation results for the largest undetected ionosphere-induced differential range error after $v_{AC}$ changes.

In the same manner, two transition points, A and B, are defined to establish the linear expression to bound $Er_{undetected}^{max}$ for the ionospheric front model under a moderate gradient. The x-coordinate of point A, i.e., $A_{\Delta v_m}^{mo}$, indicates the $\Delta v_m$ value beyond which the DSIGMA monitor is able to detect the ionospheric front. The upper bound of $Er_{undetected}^{max}$ is conservatively set as the maximum $Er_{undetected}^{max}$ when $\Delta v_m$ is smaller than or equal to $A_{\Delta v_m}^{mo}$. The y-coordinate of point B, i.e., $B_{m,Er}^{mo}$, denotes the converged $Er_{undetected}^{max}$ when $\Delta v_m$ is equal to 500 m/s.

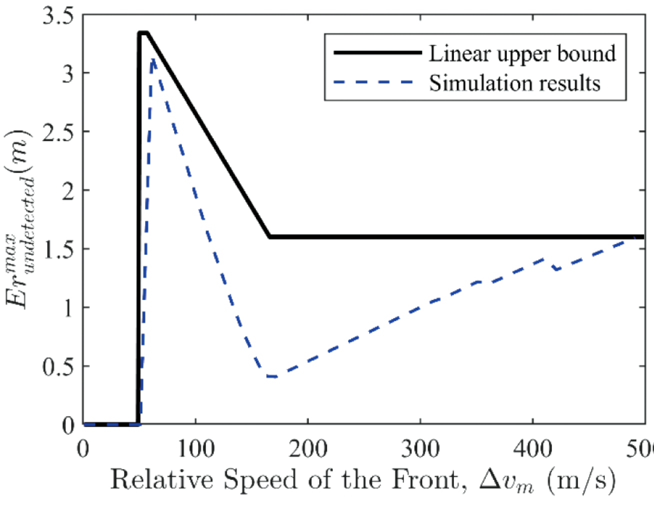


**FIGURE 17** Simulation results and linear expression for g=500 mm/km and $v_{AC}$=82.8 m/s in the ionospheric front model for the ahead case

The linear closed-form expression for $Er^{max}_{undetected}$ in the ionospheric front model with a moderate gradient can be expressed as follows:

$$Er^{max}_{undetected}(\Delta v_m) = \begin{cases} A^{mo}_{m,Er} & 0 < \Delta v_m \le A^{mo}_{\Delta v_m} \\ Er^{de}\left(\Delta v_m, A^{mo}_{\Delta v_m}, B^{mo}_{\Delta v_m}, A^{mo}_{m,Er}, B^{mo}_{m,Er}\right) & A^{mo}_{\Delta v_m} < \Delta v_m \le 500 \end{cases} \quad (55)$$

where the superscript *mo* indicates the moderate gradient condition and $B^{mo}_{\Delta v_m}$ is 500 m/s.

$A^{mo}_{m,Er}$ and $B^{mo}_{m,Er}$ are determined as a function of $g$ by a fitting method using the simulation results:

$$A^{mo}_{m,Er} = 0.0092g + 0.3818,\ B^{mo}_{m,Er} = 0.0033g + 0.0007 \quad (55)$$

$A^{mo}_{\Delta v_m}$ can also be expressed as a function of $g$ with the fitting method:

$$A^{mo}_{\Delta v_m} = -0.8594g + 382.9 \quad (56)$$

The simulation results and closed-form linear expression as a function of $\Delta v_l$, $g_1$, and $g_2$ for the plasma bubble model are shown in Figure 18. The established linear expression needs to bound $Er^{max}_{undetected}$ induced by the two gradients of the plasma bubble model. Similar to the linear expression established for the ionospheric front model, the results and linear expression are divided into two parts. One component corresponds to severe gradients, when at least one of the two gradients is larger than or equal to $\mathrm{MDG}_{igm}$ (250 mm/km). The second component corresponds to moderate gradients, when the magnitudes of both gradients are smaller than 250 mm/km.

For severe gradients, a large $Er^{max}_{undetected}$ is induced in the behind case, where the ground is affected by the plasma bubble earlier than the aircraft when $\Delta v_l$ is small. As $\Delta v_l$ becomes larger, the largest $Er^{max}_{undetected}$ occurs in the ahead case when one of the two gradients is smaller than $\mathrm{MDG}_{igm}$. When $\Delta v_l$ becomes sufficiently large, $Er^{max}_{undetected}$ converges to a value proportional to the magnitude of the larger of the

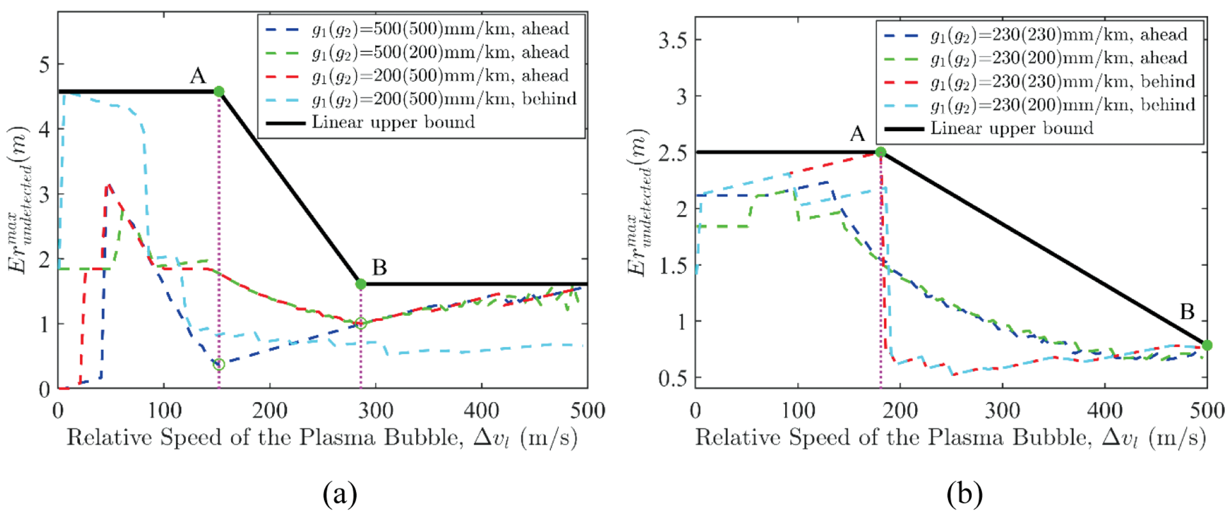


**FIGURE 18** Example of a linear expression as a function of $\Delta v_l$, $g_1$, and $g_2$ for the plasma bubble model (a) Plasma bubble model with severe gradients (b) Plasma bubble model with moderate gradients

two gradients. For moderate gradients, $Er_{undetected}^{max}$ increases to its maximum and starts to decrease when the plasma bubble can be detected by the DSIGMA monitor.

Points A and B are defined as two transition points for the linear expression of $Er_{undetected}^{max}$:

$$Er_{undetected}^{max}(\Delta v_l) = \begin{cases} A_{l,Er}^{se} & 0 < \Delta v_l \le A_{\Delta v_l}^{se} \\ Er\left(\Delta v_l, A_{\Delta v_l}^{se}, B_{\Delta v_l}^{se}, A_{l,Er}^{se}, B_{l,Er}^{se}\right) & A_{\Delta v_l}^{se} < \Delta v_l \le B_{\Delta v_l}^{se} \\ B_{l,Er}^{se} & B_{\Delta v_l}^{se} < \Delta v_l \le 500 \end{cases} \tag{57}$$

where the subscript $l$ indicates the plasma bubble model. $A_{\Delta v_l}^{se}$ is equal to $A_{\Delta v_m}^{se}$ defined for the ionospheric front model under severe gradients. $A_{l,Er}^{se}$ and $B_{l,Er}^{se}$ are determined by the fitting method:

$$A_{l,Er}^{se} = 0.00918 g_{max}, \quad B_{l,Er}^{se} = 0.00314 g_{max} \tag{58}$$

where $g_{max} = \max\{g_1, g_2\}$ is the larger of the two gradients for the plasma bubble model.

$B_{\Delta v_l}^{se}$ is also determined by the fitting method:

$$B_{\Delta v_l}^{se} = -0.4686 g_{max} + 511.22 \tag{59}$$

Similarly, the explicit expression for $Er_{undetected}^{max}$ under moderate gradients can be expressed as follows:

$$Er_{undetected}^{max}(\Delta v_l) = \begin{cases} A_{l,Er}^{mo} & 0 < \Delta v_l \le A_{\Delta v_l}^{mo} \\ Er\left(\Delta v_l, A_{\Delta v_l}^{mo}, B_{\Delta v_l}^{mo}, A_{l,Er}^{mo}, B_{l,Er}^{mo}\right) & A_{\Delta v_l}^{mo} < \Delta v_l \le 500 \end{cases} \tag{60}$$

where $A_{l,Er}^{mo}$ and $B_{l,Er}^{mo}$ are determined by the fitting method using simulation results:

$$A_{l,Er}^{mo} = 0.0092 g_{max} + 0.3818, \quad B_{l,Er}^{mo} = 0.0033 g_{max} + 0.0007 \tag{61}$$

Here, $B_{\Delta v_l}^{mo}$ is 500 m/s, and $A_{\Delta v_l}^{mo}$ is determined as a function of $g_{max}$ by the fitting method:

$$A_{\Delta v_l}^{mo} = -0.5 g_{max} + 301 \tag{62}$$

## 5.1 | Comparison Between GAST-C and GAST-D

The linear expressions of $Er_{undetected}^{max}$ for GAST-C and GAST-D are compared in Figure 19. The blue solid line and red dashed line represent the linear expressions for GAST-C and GAST-D, respectively, for the ionospheric front model with $g = 500$ mm/km. The green dashed line shows the linear expression of GAST-D for the plasma bubble model with $g_1 = 500$ mm/km and $g_2 = 500$ mm/km. The linear closed-form expression of GAST-C for the ionospheric front model was obtained from Kim et al. (2021).

As shown in Figure 19, due to the small divergence rate induced by the near-stationary ionospheric front, it is difficult for the CCD monitor to detect these fronts in GAST-C (Luo et al., 2005). Therefore, $Er_{undetected}^{max}$ reaches a maximum under slow-moving ionospheric fronts. In contrast, GAST-D applies an additional

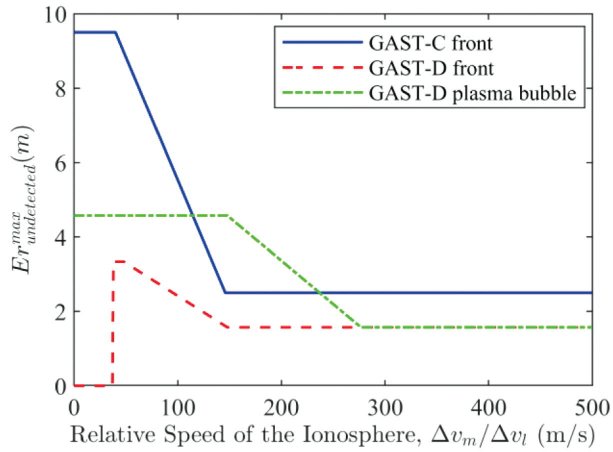


**FIGURE 19** Comparison of linear expressions between GAST-C and GAST-D

DSIGMA monitor, and thus, the near-stationary ionospheric fronts are well detected without $Er_{undetected}$ generated. However, it should be noted that for the plasma bubble model, $Er^{max}_{undetected}$ can still reach several meters when $\Delta v_l$ is small. Besides the DSIGMA and CCD monitors, GAST-D applies an IGM on the ground to directly detect the ionospheric gradient. Moreover, GSAT-D utilizes a smaller time constant of 30 s in the CSC filter. The additional ionospheric monitors and reduced CSC filter time constant largely reduce the delay effect and result in a decrease of 38% for $Er^{max}_{undetected}$ when $\Delta v_m$ and $\Delta v_l$ are sufficiently large.

The results in Pullen et al. (2017) show that $Er^{max}_{undetected}$ can be bounded by 2.75 m under a mid-latitude ionospheric front, whereas our linear expression shows that $Er^{max}_{undetected}$ can be as large as 3.34 m. The main reason for this inconsistency is that a speed profile defined in ICAO Annex 10 is used in Pullen et al. (2017), while a constant aircraft speed is adopted in this research. With a constant aircraft speed, the DSIGMA monitor cannot take advantage of aircraft speed changes. This also explains why relatively large range errors occur when the speed of an ionospheric anomaly is close to the aircraft speed. This increase in range error is disadvantageous because it may impact the service availability. However, the availability reduction is limited to the condition in which the anomaly speed is close the aircraft speed.

## 6 | CONCLUSION

This paper has established linear closed-form expressions to bound the $Er^{max}_{undetected}$ induced by ionospheric anomalies for GAST-D under threat models for an ionospheric front and plasma bubble. In GAST-D GBAS, geometry screening is transferred from the ground station to the aircraft to obtain higher availability. The GAST-D geometry screening in the aircraft system requires $E_{IG}$, which is computed from a linear combination of the up-linked parameters $Y_{EIG}$ and $M_{EIG}$. Because $E_{IG}$ must bound all predetermined potentially $Er^{max}_{undetected}$ values, the established expressions can be used to help determine $Y_{EIG}$ and $M_{EIG}$ for each runway threshold.

The expressions are divided into two parts to bound $Er^{max}_{undetected}$ under severe and moderate gradients. Under severe gradients, near-stationary ionospheric fronts can be fully mitigated by the DSIGMA monitor, whereas slow-moving plasma bubbles are likely to induce an $Er_{undetected}$ of several meters. Under moderate gradients, an expression is determined as a decreasing linear function when the DSIGMA monitor is able to detect the anomaly. The established expression can be applied to the development of GAST-D operation for mid-latitude and low-latitude regions. Previous results with GAST-C show vulnerability in defending against near-stationary ionospheric fronts. The additional DSIGMA monitor in GAST-D greatly improves the mitigation of such cases under severe gradients. In addition, the smaller time constant used in the CSC filter reduces the time-delay impact on ionospheric errors. The derived linear expressions depend on the assumed ionospheric threat models and given monitor thresholds, and a constant aircraft speed is used in the derivation. Further study will involve aircraft speed profiles, as defined in ICAO Annex 10.

## ACKNOWLEDGMENTS

We gratefully acknowledge support from Research Grants Council (RGC) (grant no. 25202520) and National Natural Science Foundation of China (NSFC) (grant no. 42004029), which funded this work.

## CONFLICT OF INTEREST

The authors declare no potential conflicts of interest.

## REFERENCES

Chang, H., Yoon, M., Pullen, S., Marini-Pereira, L., & Lee, J. (2021). Ionospheric spatial decorrelation assessment for GBAS daytime operations in Brazil. *NAVIGATION, 68*(2), 391–404. https://doi.org/10.1002/navi.418

Hatch, R. (1982). The synergism of GPS code and carrier measurements. *Proc. of the 3rd International Geodetic Symposium on Satellite Doppler Positioning, Vol 2.* 1213–1232.

Hoffmann, H. O., & Walton, R. O. (2018). Integration of the ground-based augmentation system in continuous descent operations. *NAVIGATION, 65*(4), 571–580. https://doi.org/10.1002/navi.262

ICAO. (2018). Standards and recommended practices, Annex 10 to the Convention on International Civil Aviation, amendment 92*, International Civil Aviation Organization (ICAO).*

Khanafseh, S., Yang, F., Pervan, B., Pullen, S., & Warburton, J. (2012). Carrier phase ionospheric gradient ground monitor for GBAS with experimental validation. *NAVIGATION, 59*(1), 51–60. https://doi.org/10.1002/navi.3

Kim, D., Yoon, M., Lee, J., Pullen, S., & Weed, D. (2017). Monte Carlo simulation for impact of anomalous ionospheric gradient on GAST-D GBAS. *Proc. of the ION 2017 Pacific PNT Meeting,* Honolulu, HI. 47–55. https://doi.org/10.33012/2017.15049

Kim, D., Yoon, M., Pullen, S., & Lee, J. (2021). Closed-form analysis of undetected range errors due to ionospheric impacts for GBAS category I operations. *NAVIGATION, 68*(3), 507–519. https://doi.org/10.1002/navi.442

Konno, H. (2007). Dual-frequency smoothing for CAT III LAAS: Performance assessment considering ionosphere anomalies. *Proc. of the 20th International Technical Meeting of the Satellite Division of the Institute of Navigation (ION GNSS+ 2007),* Fort Worth, TX. 424–437. https://www.ion.org/publications/abstract.cfm?articleID=7457

Lee, J., Luo, M., Pullen, S., Enge, P., & Brenner, M. (2006). Position-domain geometry screening to maximize LAAS availability in the presence of ionosphere anomalies. *Proc. of the 19th International Technical Meeting of the Satellite Division of the Institute of Navigation (ION GNSS 2006),* Fort Worth, TX. 393–408. https://www.ion.org/publications/abstract.cfm?articleID=6900

Lee, J., Morton, Y. T. J., Lee, J., Moon, H.-S., & Seo, J. (2017). Monitoring and mitigation of ionospheric anomalies for GNSS-based safety critical systems: A review of up-to-date signal processing techniques. *IEEE Signal Processing Magazine, 34*(5), 96–110. https://doi.org/10.1109/MSP.2017.2716406

Lee, J., Seo, J., Park, Y., Pullen, S., & Enge, P. (2011). Ionospheric threat mitigation by geometry screening in ground-based augmentation systems. *Journal of Aircraft, 48*(4), 1422–1433. https://doi.org/10.2514/1.C031309

Lee, J., Yoon, M., Pullen, S., Gillespie, J., Mather, N., Cole, R., de Souza, J. R., Doherty, P., & Pradipta, R. (2015). Preliminary results from ionospheric threat model development to support GBAS operations in the Brazilian region. *Proc. of the 28th International Technical Meeting of the Satellite Division of the Institute of Navigation (ION GNSS+ 2015),* Tampa, FL. 1500–1506. https://www.ion.org/publications/abstract.cfm?articleID=13040

Luo, M., Pullen, S., Datta-Barua, S., Zhang, G., Walter, T., & Enge, P. (2005). LAAS study of slow-moving ionosphere anomalies and their potential impacts. *Proc. of the 18th International Technical Meeting of the Satellite Division of the Institute of Navigation (ION GNSS 2005),* Tampa, FL. 2337–2349. https://www.ion.org/publications/abstract.cfm?articleID=6439

Marini-Pereira, L., Pullen, S., Moraes, A. D. O., & Sousasantos, J. (2021). Ground-based augmentation systems operation in low latitudes - part 1: Challenges, mitigations, and future prospects. *Journal of Aerospace Technology and Management, 13*, 1–24. https://doi.org/10.1590/jatm.v13.1236

Misra, P., & Enge, P. (2004). *Global positioning system: Signals, measurements, and performance*. Ganga-Jamuna Press.

Pullen, S., Cassell, R., Johnson, B., Brenner, M., Weed, D., Cypriano, L., Topland, M., Stakkeland, M., Pervan, B., Harris, M., Saito, S., Lee, J., Clark, B., Beauchamp, S., & Dennis, J. (2017). Impact of ionospheric anomalies on GBAS GAST D service and validation of relevant ICAO SARPs requirements. *Proc. of the 30th International Technical Meeting of the Satellite Division of the Institute of Navigation (ION GNSS+ 2017),* Portland, OR. 2085–2105. https://doi.org/10.33012/2017.15135

Pullen, S., Park, Y. S., & Enge, P. (2009). Impact and mitigation of ionospheric anomalies on ground-based augmentation of GNSS. *Radio Science, 44*(1), 1–10. https://doi.org/10.1029/2008RS004084

Robert, E., Jonas, P., Vuillaume, J., Salos, D., Hecker, L., & Yaya, P. (2018). Development of a European ionosphere threat model in support of GBAS deployment. *Proc. of the 2018 IEEE/ION Position, Location and Navigation Symposium (PLANS),* Monterey, CA. 1181–1190. https://doi.org/10.1109/PLANS.2018.8373503

RTCA DO-253D. (2017). *Minimum operational performance standards for global positioning system local area augmentation system airborne equipment* (RTCA DO-253D).

Saito, S., & Yoshihara, T. (2017). Evaluation of extreme ionospheric total electron content gradient associated with plasma bubbles for GNSS ground-based augmentation system. *Radio Science, 52*(8), 951–962. https://doi.org/10.1002/2017RS006291

Saito, S., Yoshihara, T., & Fujii, N. (2009). Development of an ionospheric delay model with plasma bubbles for GBAS. *Proc. of the 2009 International Technical Meeting of the Institute of Navigation,* Anaheim, CA. 947–953. https://www.ion.org/publications/abstract.cfm?articleID=8377

Saito, S., Sunda, S., Lee, J., Pullen, S., Supriadi, S., Yoshihara, T., Terkildsen, M., & Lecat, F. (2017). Ionospheric delay gradient model for GBAS in the Asia-Pacific region. *GPS Solutions, 21*(4), 1937–1947. https://doi.org/10.1007/s10291-017-0662-1

Simili, D. V., & Pervan, B. (2006). Code-carrier divergence monitoring for the GPS local area augmentation system. *Proc. of 2006 IEEE/ION Position, Location, and Navigation Symposium (PLANS),* Coronado, CA. 483–493. https://doi.org/10.1109/PLANS.2006.1650636

**How to cite this article:** Li, W., & Jiang, Y. (2023). Closed-form study of undetected range errors induced by ionospheric anomalies for GAST-D GBAS. *NAVIGATION, 70*(4). https://doi.org/10.33012/navi.603